Laminar Burning Velocities of Lean Hydrogen–Air Mixtures

Kumar S. Raman

Graduate Aeronautical Laboratories
California Institute of Technology
Pasadena, CA 91125

Explosion Dynamics Laboratory Report FM97-15

January 30, 1998

Contents

List of Figures

List of Tables

1 Introduction

1.1 Overview

The laminar burning velocity (often referred to as simply the burning velocity) of a combustible mixture is defined as the relative velocity at which a flame propagates with respect to the unburned fluid and is one of the fundamental quantities characterizing combustion. Accurate measurements of the burning velocity are important for validating theoretical models and numerical simulations predicting the progress of a laminar combustion as well as in practical combustion systems (van Wingerden 1997). In particular, the burning velocities of hydrogen–air mixtures are important parameters in designing safety measures in applications where hydrogen is used as a fuel (Koroll et al. 1993).

A *flame* can be defined as a subsonic combustion wave driven by a self–propagating exothermic reaction typically characterized by a localized reaction zone separating reactants and products (Barnard and Bradley 1985; Turns 1996). A one–dimensional, steady, planar flame analysis gives insight into several important properties of laminar flames (turbulent flames are more complicated and the burning velocity is no longer a well–defined quantity; turbulent flames will not be considered in this work). Such an analysis is also valid locally for spherical flames as long as the flame thickness is small compared to the radius of curvature of the flame front.

Figure 1 shows an idealized planar flame moving with an apparent flame speed V_f in the lab frame. Although this flow is multi–component in nature, for premixed flames it is a good approximation to treat the reactants and products as uniform fluids. The subscripts u and b refer to unburned (reactant) and burned (product) fluid respectively. The laminar burning velocity is

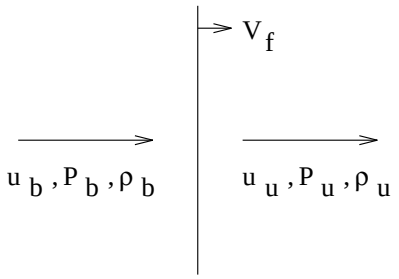

Figure 1: One–dimensional planar flame analysis.

defined as:

$$S_u \equiv V_f - u_u \tag{1}$$

S_u is a function of the reactant mixture composition, the reactant temperature and pressure, and also the existence of flow gradients or strain at the flame front. Conservation of mass across the flame implies

$$\rho_u(V_f - u_u) = \rho_b(V_f - u_b) \tag{2}$$

or in terms of S_u,

$$u_b - u_u = S_u(1 - \frac{\rho_u}{\rho_b}) \tag{3}$$

Before investigating the conservation of momentum across the flame, it is useful to examine the relative importance of the various terms in the momentum equation for our particular flow. We can estimate the Reynolds number of our flow by using the density and viscosity of air at room

temperature and taking as the characteristic velocity, a typical value of S_u for a lean mixture of hydrogen and air as measured in this experiment. Since spherical flames were the focus of the present work, a relevant length scale would be the diameter of the flame kernel at the instant S_u was measured. Using these numbers:

$$\mu(T = 300K) \sim 1.8 \times 10^{-5} \quad \text{kg/(ms)} \tag{4}$$

$$\rho(T = 300K) \sim 1.2 \quad \text{kg/m}^3 \tag{5}$$

$$S_u \sim 10 \quad \text{cm/s} \tag{6}$$

$$L \sim 30 \quad \text{cm} \tag{7}$$

$$Re \equiv \frac{\rho U L}{\mu} \sim 2000 \tag{8}$$

At later times in the flow, the velocity induced by the buoyant motion of the flame can be as much as 1 m/s, yielding a Reynolds number of 2 $\times 10^4$. These values imply that in the regions away from the flame sheet and the walls of the vessel, viscous shear stresses are negligible compared to inertia. Near the flame sheet, a more important characteristic length would be the flame thickness δ which would yield $Re \sim 1$. However, if the velocity gradients are modest in the vicinity of the flame, then shear stress can also be ignored in computing the structure of the flame. This is the case in the present study since we only consider laminar flames propagating in a quiescent mixture. The flow gradients are primarily in the normal direction resulting in a viscous stress that is very small compared to the pressure.

Gravitational forces are very important in the present flow since the combustion products are much lighter than the reactants. The buoyant products rise upwards, distorting the initially spherical flame surface and inducing a substantial flow in the surrounding reactants. However, the material elements within the flame are uniformly accelerated so that the local structure of the flame is unaffected. Therefore, the direct effect of gravitational forces can be ignored in considering the *local* structure of the flame.

Incorporating these simplifications, neglecting viscous stresses and gravity, into the conservation of momentum across the flame implies:

$$P_u + \rho_u S_u^2 = P_b + \rho_b (S_u + u_u - u_b)^2 \tag{9}$$

Notice that we have solved for the velocity change $u_b - u_u$ in Eq. 2. Substituting in the previous equation yields:

$$P_u = P_b + S_u^2 (\frac{\rho_u}{\rho_b})(\rho_b - \rho_u) \tag{10}$$

It is useful to non–dimensionalize Eq. 10:

$$\frac{P_u}{\rho_u c_u^2} = \frac{P_b}{\rho_u c_u^2} + M_u^2 (1 - \frac{\rho_u}{\rho_b}) \tag{11}$$

where $M_u \equiv S_u / c_u$ is the upstream Mach number based on the upstream sound speed. We can estimate the size of the left hand term by using $P_u = 1$ bar, $c_u \sim 343$ m/s, and the density of air at room temperature which is about 1.2 kg/m^3.

$$\frac{P_u}{\rho_u c_u^2} \sim \frac{10^5}{1.2 \times 343^2} \sim 0.7 \sim 1 \tag{12}$$

So the left hand side is of order unity. In the present experiments, the maximum value of M_u = 0.001. Therefore, the second term is negligible in comparison to the left hand side (it should be noted that the density ratio is not large enough to compensate for the low Mach number). Therefore, we come to the conclusion that the pressure is essentially constant across a (sufficiently slow) laminar flame.

$$P_u \approx P_b \tag{13}$$

Applying the same type of analysis on the energy equation, we find that the contributions of gravity, viscosity and kinetic energy are negligible in a slow flame. There is no heat addition immediately across the flame front (the chemical reaction occurs within the flame). With these simplifications, conservation of energy across the flame front implies:

$$h_u = h_b \tag{14}$$

However, within the flame itself, there are gradients in temperature and species. The balance between diffusion, convection and energy release is what produces the self-sustaining structure of the flame. Ahead of the energy release region, this balance can be approximated as

$$\rho S_u c_p \left(T_b - T_u\right) \approx j_q \tag{15}$$

where j_q is the heat flux. This form of the energy equation can give an estimate of the reaction zone thickness. The heat flux j_q has contributions from conduction and radiation. Assuming that radiation is negligible and that Fourier's law holds:

$$j_q = -k\frac{dT}{dx} \tag{16}$$

where k is the thermal conductivity of the mixture. If we assume that the temperature change is linear across the flame, then:

$$\frac{dT}{dx} \approx \frac{T_b - T_u}{\delta} \tag{17}$$

Combining Eqs. 15-17 gives an estimate for the reaction zone thickness δ.

$$c_p(T_b - T_u) \sim \frac{k(T_b - T_u)}{\delta \rho_u S_u} \tag{18}$$

$$\delta \sim \frac{k}{c_p \rho_u S_u} \tag{19}$$

Or introducing the thermal diffusivity κ,

$$\kappa \equiv \frac{k}{c_p \rho_u} \tag{20}$$

$$\delta \sim \frac{\kappa}{S_u} \tag{21}$$

Typical values for δ are presented in Table 1.

For the temperatures and pressures encountered in the present experiment, the ideal gas equation of state is an excellent approximation.

$$P = \rho R_g T \tag{22}$$

The temperature increases across a flame due to the energy release associated with the combustion. The increase in temperature depends strongly on the concentration of fuel. For a stoichiometric mixture, the temperature can increase by a factor of up to 6 to 8 for hydrocarbon fuels. This fact, along with Eqs. 13 and 22, implies that the density decreases by a factor of 6 to 8 across a flame in a stoichiometric mixture. In very lean H_2–air flames, the temperature rise is much smaller, as low as 2 to 3 times the initial reactant temperature. Equation 3 implies that the fluid velocity decreases across the flame front from the unburned gas region to the burned gas region as the density ratio ρ_u/ρ_b is greater than 1. A table of the combustion properties of lean hydrogen-air mixtures is found in Appendix A.

Accurate measurements of hydrogen–air burning velocities have been made over a wide range of fuel concentrations using several different methods. These methods are based on measurements of flame or fluid motion in either steady or unsteady flows.

Steady flow techniques measure S_u directly by making the flame stationary ($V_f = 0$) through stabilization on a burner, e.g. a Bunsen or Powell–type burner. Measurements of the fluid velocity u_u upstream of the flame give S_u. Burner techniques are often unsuitable for extremely lean flames due to energy (heat) loss to the burner. Steady techniques are also unsuitable for flames with cellular instability due to the difficulty in stabilizing the flame on a burner. Unsteady techniques measure S_u by measuring the flame speed V_f and inferring the laminar burning velocity by assuming a value for the fluid velocity on one side of the flame; by assuming a value for the density drop across the flame front; or by measuring the velocity of the unburned gas. Buoyancy–induced fluid motion is an important issue with unsteady techniques though such effects can be made small in a microgravity environment. Deformation of the flame front in extremely lean flames is an important issue with unsteady techniques relying on photographing the flame front to obtain a flame speed. A survey of several commonly used techniques to determine the burning velocity is presented in Andrews (1972).

The laminar burning velocity is typically less than 3 m/s for hydrogen–air mixtures and less than 40 cm/s for hydrocarbon–air mixtures. Measured values of S_u in hydrogen–air mixtures are shown in Fig. 2 as a function of hydrogen concentration. S_u is a strong function of fuel concentration varying from a maximum value of around 3 m/s at 42% hydrogen to less than 4 cm/s near the lean flammability limit at 4% hydrogen.

The present study examines the regime of H_2–air flames with H_2 concentrations less than 10% for which limited data is available due to the difficulties discussed earlier. These extremely lean hydrogen–air flames are of particular interest because of the peculiar behavior near the lean limit. The existing kinetic models for H_2–air combustion fail in the extremely lean regime while working quite well near stoichiometric. Egolfopoulos and Law (1990) suggested that this was due to a fundamental change in the combustion mechanism as different elementary reactions become important at the low temperatures encountered in lean hydrogen combustion. The combustion temperatures encountered in lean hydrogen–air flames are significantly less than with other fuels because hydrogen burns at leaner concentrations than other fuels due to its high diffusivity relative to air. Reliable experimental data for the lean combustion characteristics of hydrogen are necessary for the motivation and validation of theories explaining this peculiar behavior. This present effort aims to establish reliable experimental data for the laminar burning velocities of very lean hydrogen–air mixtures.

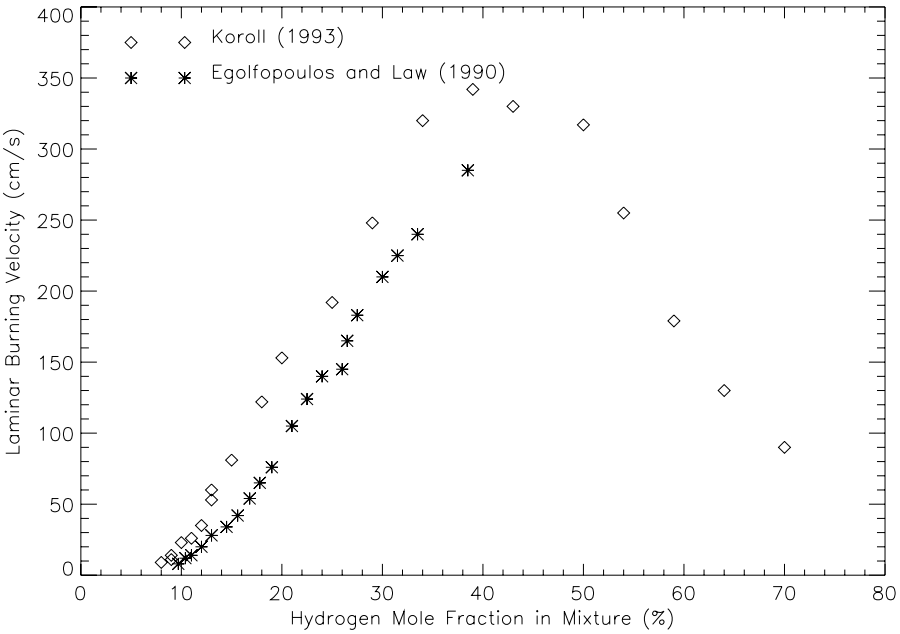

Figure 2: S_u vs hydrogen molar concentration.

1.2 Previous work

Egolfopoulos and Law (1990) used a nozzle–burner counterflow method to make measurements from 9% (lean) to 35% (moderately rich) H_2 molar concentration. This is a steady flow method which involves "the establishment of two symmetrical, planar, nearly–adiabatic flames in a nozzle–generated counterflow". From LDV measurements along the centerline of the flow, they were able to determine S_u. Details regarding this procedure are given in Egolfopoulos and Law (1990).

Koroll (1993) obtained measurements from 10% to 70% H_2 using a double–kernel method which involves igniting the reactant mixture at two ends of a combustion vessel simultaneously. At the instant the two flame fronts coincide, $u_u = 0$. Koroll recorded the two flame kernels approaching one another using a high speed schlieren video. From the schlieren movie, V_f and therefore, S_u was determined.

Ross and Shepherd (1996) used a variation on the "soap–bubble" method to measure the burning velocity near the lean flammability limit from 4% to 9% H_2. The method involved igniting the reactant mixture at the center of a large volume vessel and filming a schlieren movie of the expanding flame. Ross measured the horizontal growth of the flame kernel as a function of time (see Fig. 1.2 in (Ross and Shepherd 1996)) and fit his data to a linear function. The slope of his distance–time curve was interpreted as the flame speed V_f. Ross observed that despite buoyancy effects, his distance–time curve was very linear. He concluded that while buoyancy clearly affects the vertical growth of the flame kernel, the horizontal growth appears to be unaffected. Ross determined S_u from his flame speed measurement by assuming the burned gas was stationary ($u_b = 0$), the pressure remained constant during the measurement period, and the flame was adiabatic. He determined ρ_u/ρ_b from a constant pressure, constant enthalpy, STANJAN (Reynolds 1986) calculation and used Eq. 2 to obtain S_u.

Ronney (1990) obtained measurements near the flammability limit from 4.5% to 8% H_2 using a technique similar to Ross but under microgravity conditions. Ronney filmed the flame expansion using a motion picture camera instead of a schlieren system due to experimental constraints with his microgravity apparatus. H_2–air flames emit very little radiation so an additive, CF_3Br, was added for visibility. Ronney noted that while CF_3Br, being a combustion inhibitor, "clearly influences flame chemistry, it is believed that it has little qualitative effect on the near–limit behavior of H_2–air flames". Ronney indicated that in order to make quantitative comparisons of the experimental results with theory, it would be advantageous to eliminate the visibility agent and install a schlieren or infrared imaging system in the microgravity test section.

The double–kernel method appears to give accurate results for S_u over most of the H_2 concentration range. However, due to cellular instability and increased flame thickness, the method is unsuitable for studying flames near the flammability limit. Table 1 (Gaydon and Wolfhard 1960) gives order of magnitude values for the flame thickness as a function of burning velocity (which increases monotonically with concentration for lean mixtures). The flame thickness is relatively large for lean hydrogen flames where the burning velocity is less than 10 cm/s. Koroll noted that

S_u	Flame thickness
10 m/s	2.7 x 10^{-3} cm
1 m/s	2.7 x 10^{-2} cm
10 cm/s	0.27 cm
1 cm/s	2.7 cm

Table 1: Order–of–magnitude variation of flame thickness with burning velocity.

his data point at 10% H_2 had a ±30% error. At lower H_2 concentrations, "an overall deterioration of the flame surface" prevented any reliable data from being taken. The nozzle–burner technique seems to work well for lean flames but the near–limit behavior was not the focus of the Egolfopoulos and Law study.

The only existing data near the lean flammability limit are the results of Ross and Ronney. Ross's values for S_u are substantially higher than Ronney's. It is unclear whether this is due to the additive Ronney used or buoyancy effects; both would produce the observed trend. The reliability of Ross's data needs verification given that several assumptions were made, most notably that $u_b = 0$. In addition, there were not many data points taken as H_2–air was not the main focus of the Ross study.

The present effort was undertaken to provide an alternative to the previous methods that can be used with buoyant flames in general. It is the goal of this study to measure the burning velocity for H_2–air mixtures under normal gravity conditions near the lean flammability limit. The experimental methodology is presented in the next section followed by discussion of results and comparison with existing data.

2 Experimental Apparatus and Measurement Techniques

2.1 11–Liter Combustion Vessel

The experiments were performed in MiniCONVOL (MCV), an 11.25–ℓ rectangular combustion vessel with approximate outside dimensions 10.5–in x 10.5–in x 12.5–in. The rectangular box is

formed from four, one–inch thick, steel plates for the sides and two steel cap pieces for the top and bottom. The vessel has two window ports in which are mounted one–inch thick, BK–7 glass windows. The vessel also has two side pieces for the three gas lines and instrumentation. A diagram of MCV is given in Fig. 3.

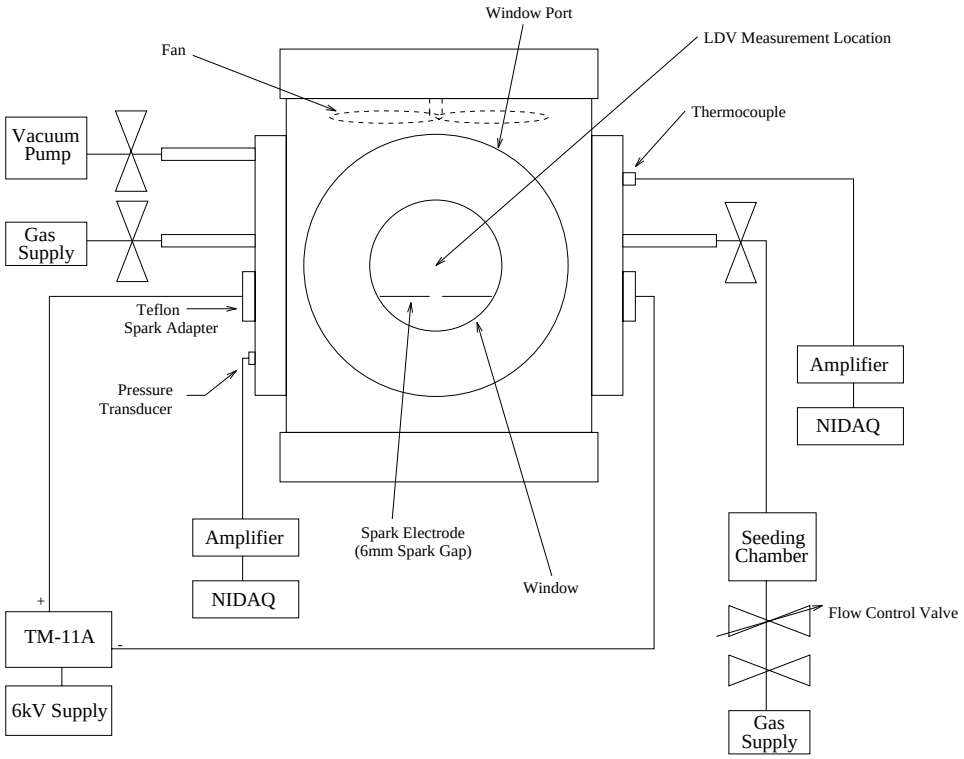

Figure 3: Diagram of MiniCONVOL 11.25–ℓ test vessel.

One of the gas lines is connected to a Sargent–Welch rotary pump and is used for evacuating the vessel and exhausting the combustion products after a burn. Another gas line is connected directly to the gas supply while the third gas line passes through a seeding chamber containing submicron alumina powder. A flow control valve regulates the density of seeding particles in the test vessel.

MCV is equipped with a Kulite model XTME–190–250A piezoelectric pressure transducer with an accuracy of ± 2.5 kPa and an Omega K type thermocouple. The pressure transducer and thermocouple signals are amplified and converted to pressure and temperature readings through a National Instruments Data Acquisition (NIDAQ) AT-MIO-64E-3 multi–purpose board sampling at a rate of 1000 measurements per second. The board is controlled by a LabView computer interface.

A mixing fan is mounted on the top cap to mix the reactants prior to ignition. Two electrical feedthroughs meet at the center of MCV from opposite sides with a 6 mm spark gap. Each ignitor is mounted into a Teflon spacer to insulate the ignitor from the walls of the vessel. The power for the spark is provided by a 6 kV Hipotronics power supply connected to a TM–11A Trigger Module. The TM–11A is triggered by a fire button on the control panel which also starts the computer data acquisition system.

MCV uses the same gas handling, electrical, data acquisition, and vacuum systems as the CONVOL 400–ℓ Combustion Facility. A more detailed description of these systems is given in Ross

(1996).

2.2 4–Beam He/Ne Photodiode System

The original intention was to measure V_f using an optical system similar to that of Hamamoto (1991) who combined this with an LDV to measure burning velocities of propane–air mixtures (see Fig. 4).

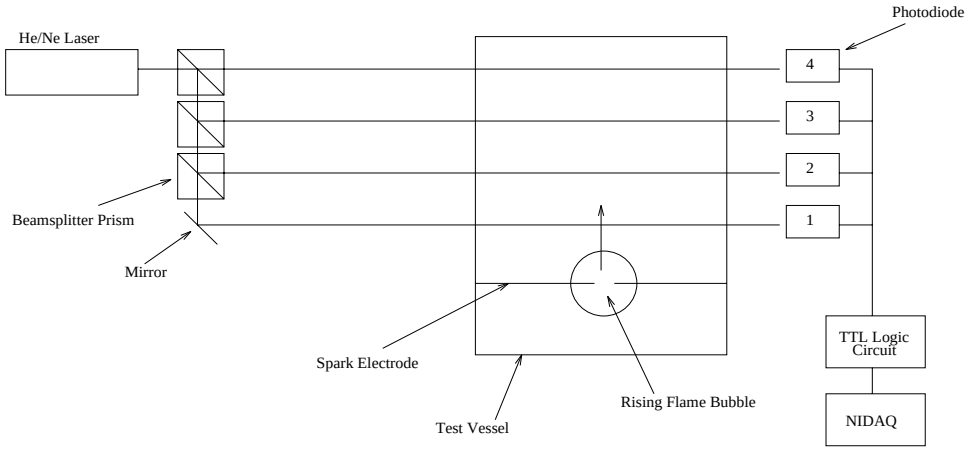

Figure 4: Four beam photodiode technique to determine V_f.

The basic design is that a He/Ne laser beam is split into four parallel beams by three beamsplitter prisms and a mirror. The beamsplitters and mirrors are on adjustable mounts and adjusted so that the four beams pass through the test vessel, above the spark gap, and shine on respective photodiode detectors. Each detector is connected to a TTL output circuit with TTL low (0 V output) corresponding to the beam shining on the detector and TTL high (5 V output) corresponding to the beam being blocked. The four TTL outputs are connected to the NIDAQ board and monitored with the LabView computer interface, both of which were described earlier.

The operation of the system is as follows. As the flame kernel expands, the four beams would be blocked consecutively and the respective TTL outputs would momentarily go high. These four 5V pulses would be recorded by the data acquisition system and from the time between pulses and the distances between the beams, a flame speed V_f could be determined from the slope of a linear fit.

It turned out that this system was not reliable and the schlieren system described in the next section was used to obtain the flame speed V_f. Probable reasons for the failure include problems with alignment or electronics. *Beam steering*, the deflection of the laser beams due to the changing index of refraction as the flame approaches, may have also played a role. Beam steering is a relevant issue in LDV as will be discussed. Schlieren photography, described in the next section, exploits beam steering to generate a picture of the density gradient within a flame.

2.3 Video Color Schlieren System

The schlieren system shown in Fig. 5 was used to measure the apparent flame speed V_f.

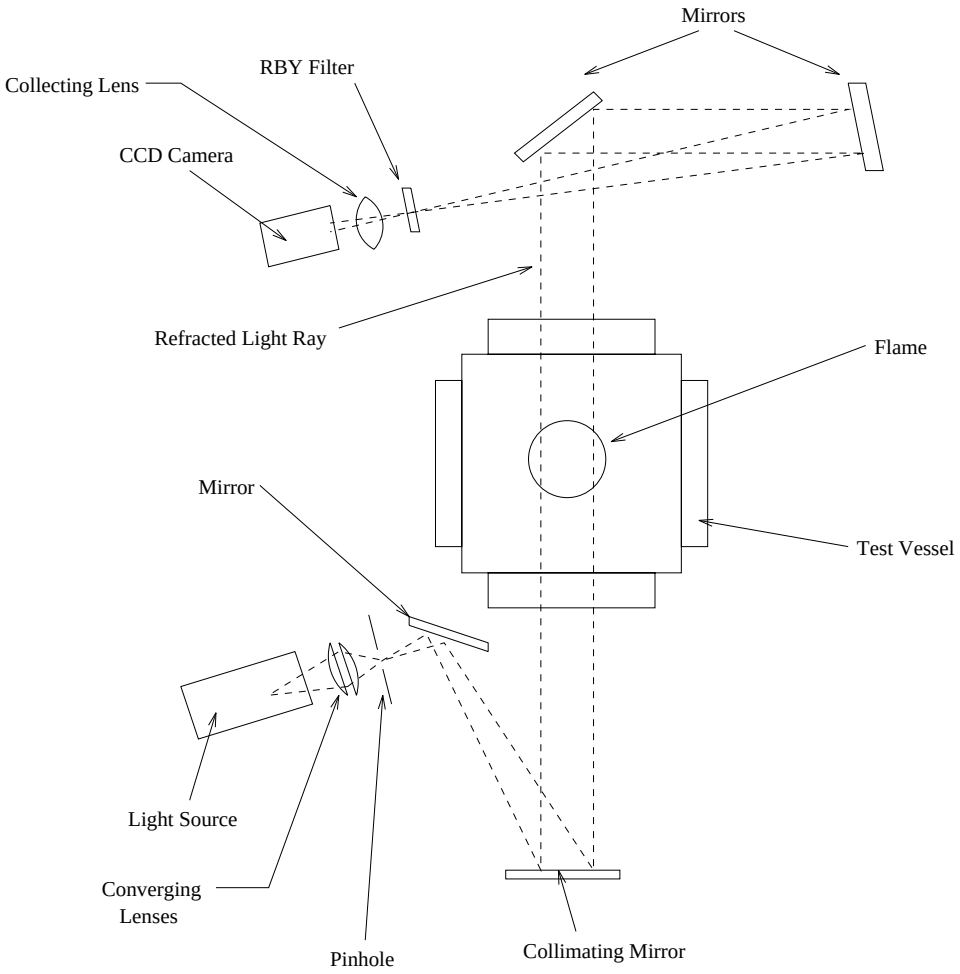

Figure 5: Video schlieren system for determining the flame speed, V_f.

Light rays from an Oriel continuous filament lamp pass through a pair of converging lenses to focus on a pinhole producing a spherically diverging beam (i.e. an effective point source is created). The beam reflects off a collimating mirror producing parallel light rays that pass into the test section. The individual light rays are refracted by varying amounts due to the index of refraction gradient, which for gases is proportional to the density gradient, caused by the flame. After passing through the test section, the light is focused on a three–color filter with red, blue, and yellow regions. The system is aligned so that if a light ray is not refracted in the test section, it will pass through the center of the filter while refracted light rays will pass through either the red, blue, or yellow section of the filter depending on the direction of refraction.

A CCD camera is placed after the color filter and images the inside of the test vessel. If a large fraction of light rays passing through a particular region of the test vessel are refracted into the yellow section of the filter, then that corresponding region will appear yellow on the schlieren movie; similarly for the red and blue sections. Regions of the test vessel where the density gradient is large appear as high contrast regions on the schlieren photograph while regions where the density gradient is small appear as low contrast regions on the photograph. Therefore, the schlieren photograph is a photograph of the density gradient field within the test vessel where contrast represents magnitude and color represents direction. For the purposes of this experiment,

only the magnitude was needed and using a knife edge instead of a color filter, as in Ross (1996), would have been equally as appropriate. In fact, a knife edge may have been the better choice for obtaining a sharp, monochromatic image.

Since the density gradient is very large across the flame front, the flame front will be identified as a bright boundary on the schlieren photograph. Examples of schlieren photographs are given in Figs. 13 and 17. The time between frames is 1/60 Hz or approximately 17 ms (note that every fourth frame is given in Figure 17 so the time between frames shown is 68 ms). The upward motion of the flame was measured using the top of the flame as the reference point as shown in Fig. 6.

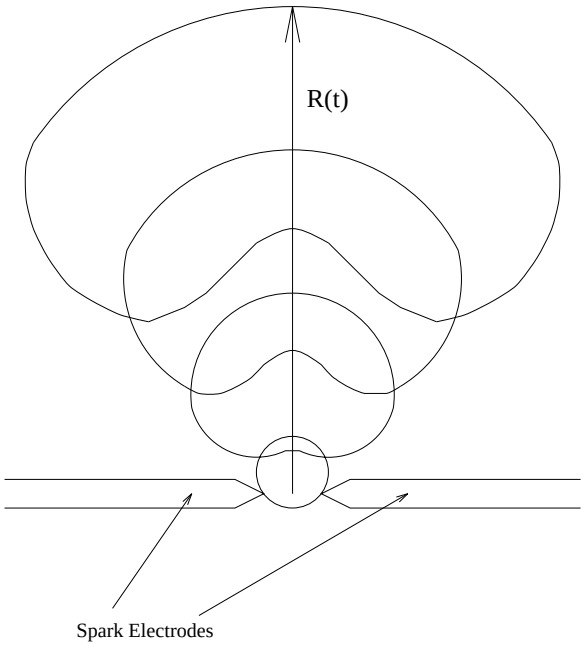

Figure 6: Measuring the upward motion of a rising flame.

The position vs. time data was numerically differentiated using a three point Lagrangian interpolation routine that was part of the PV–WAVE data analysis software package. The differentiated data was interpreted as the apparent flame speed as a function of time. The flame speed used to calculate the burning velocity was this function evaluated at the time the flame arrived at the LDV measurement location. This issue is discussed in greater detail in subsequent sections.

2.4 Laser Doppler Velocimeter

The most important diagnostic in this experiment is the Laser Doppler Velocimeter (LDV) (Durst et al. 1976; Drain 1980; VKI 1991) which is used to measure u_u (see Fig. 7). The system consists of three major components: a Spectra Physics Model 168b argon ion laser, DANTEC optics, and a DANTEC counter processor.

The Ar–ion laser beam passes through a prism bridge and is made circularly polarized by a quarter–wave plate retarder mounted on the prism bridge. The beam is made linearly polarized by a second retarder before being split into two equal intensity beams separated by 60 mm. A 1200 mm focal length lens focuses the two beams to a single point approximately 30 mm above the spark gap. A beam waist adjustment lens ensures that the two beams cross at their beam waists. The

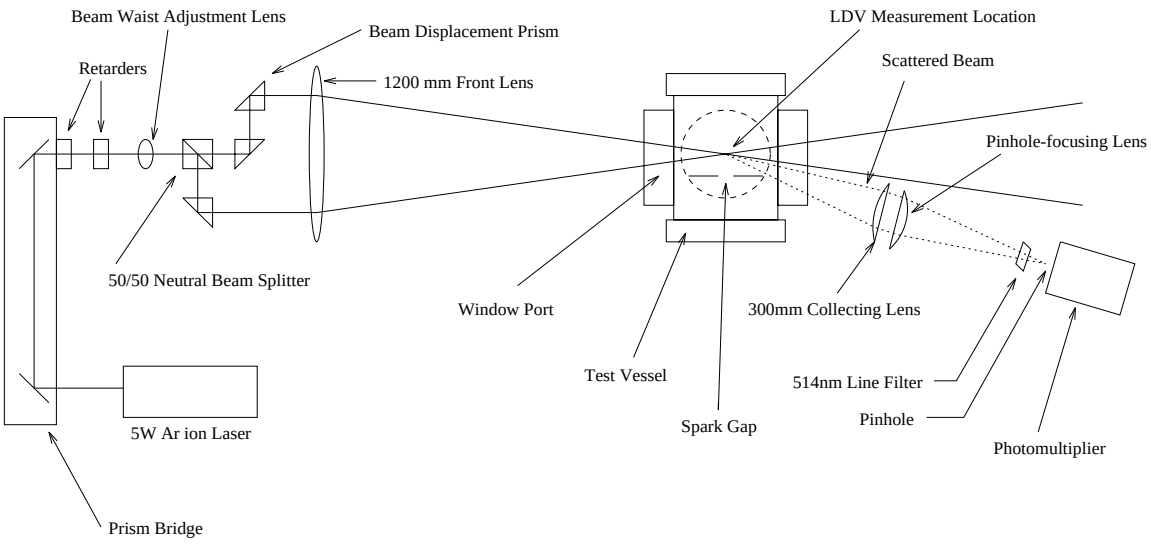

Figure 7: One–component, forward–scatter LDV system.

point at which the beams cross is called the *focal volume*. The focal volume is an ellipsoidal region with major axis on the order of 1 mm in length and minor axes on the order of 0.6 mm in length in the present experiment. The major axis lies along the optical axis while the two minor axes are perpendicular to the optical axis. The interference of the two crossed beams causes interference fringes to form in the focal volume as shown in Fig. 8. The fringe spacing d_f is given by:

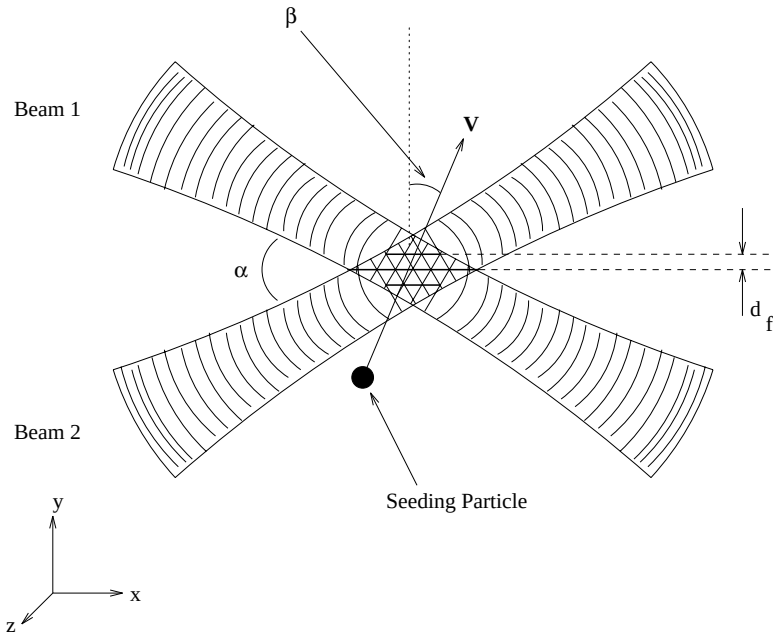

Figure 8: Interference fringes in the LDV focal volume.

$$d_f = \frac{\lambda}{2\sin(\frac{\alpha}{2})} \tag{23}$$

where λ is the wavelength, and α is the beam crossing angle. The beam crossing angle is determined

from the initial beam separation and the focal length of the front lens. In the present work, the fringe spacing is 10.28 μm.

That the two beams cross at their beam waists is important for three reasons. First, the beam waist is the unique point of a Gaussian beam where the wavefronts are planar; this means that the highest quality interference pattern is produced when the two beams cross at their beam waists. Second, the beam waist is the point of maximum light intensity (or minimum cross–sectional area) along a Gaussian beam so crossing at the beam waist maximizes the potential signal level. Third, if the beams do not cross at the beam waist, then there is a possibility that the fringe spacing may not be uniform throughout the focal volume; this can cause serious difficulties in the interpreting the output of the counter processor described below.

Collection optics are placed to one side of the optical axis as shown in Fig. 7. A 300 mm lens focused on the focal volume collects light scattered from the focal volume. A second lens focuses the collected light on a pinhole through a 514.5 nm green interference filter. The Ar–ion laser beam contains several frequencies in the blue–green range but the two dominant frequences are at 488 nm and 514.5 nm. The green wavelength at 514.5 nm was chosen because at high laser powers, it is the more powerful component; the green wavelength also gives a wider fringe spacing although the seeding particles in this experiment were so small that the 488 nm blue beam would have been equally appropriate. The pinhole-focusing lens and the pinhole are part of a single photomultiplier (PM) optics unit. The light then enters the photomultiplier tube. The PM optics unit ensures that only the light scattered from the focal volume enters the photomultiplier.

Consider a seeding particle moving through the focal volume with velocity $\mathbf{v}$ and angle β with respective to the direction orthogonal to the fringe pattern as shown in Fig. 8. As it crosses the focal volume, the particle scatters light from the fringes in its path. The reader should note that Fig. 8 is a 2–D cross section of the flow taken in the plane defined by the two laser beams. The velocity $\mathbf{v}$ is the projection of the actual 3–D velocity onto this plane. In essence, the LDV measures the velocity component orthogonal to the fringe pattern (the y–component is being measured in Fig. 8). The photomultiplier tube outputs a voltage pulse for each scattered fringe with the frequency:

$$f_D = \frac{v \cos \beta}{d_f} \tag{24}$$

where f_D is called the *Doppler frequency*. Since the beams are Gaussian beams (TEM 00), the intensity profile is Gaussian at any cross section of the beam. Therefore, the total signal obtained for a single particle crossing the focal volume will be a collection of pulses spaced with a frequency f_D and enveloped by a Gaussian curve (see Fig. 9). This collection of pulses is called a *Doppler burst*.

Figure 9 is the signal obtained directly from the photomultiplier in an ideal experiment. The only noise present would be the photomultiplier shot noise which can be made small but never eliminated. In a real experiment, the photomultiplier signal has low frequency components that cause a zero offset. A real PM signal is shown in the first frame of figure 10. This offset is called the *Doppler pedestal*. The pedestal is a result of unequal power in the two beams causing an imperfect interference pattern, e.g. regions of destructive interference would still have a small amount of light intensity. With some signal processing methods, the pedestal does not pose a problem but with frequency counting, the method used in the present experiment, the pedestal must be removed. Improving the quality of the optical components will make the pedestal small but nonzero. If the frequencies due to the pedestal are on the order of the expected Doppler frequencies, then a frequency shifting device, such as a Bragg Cell, must be used to separate the

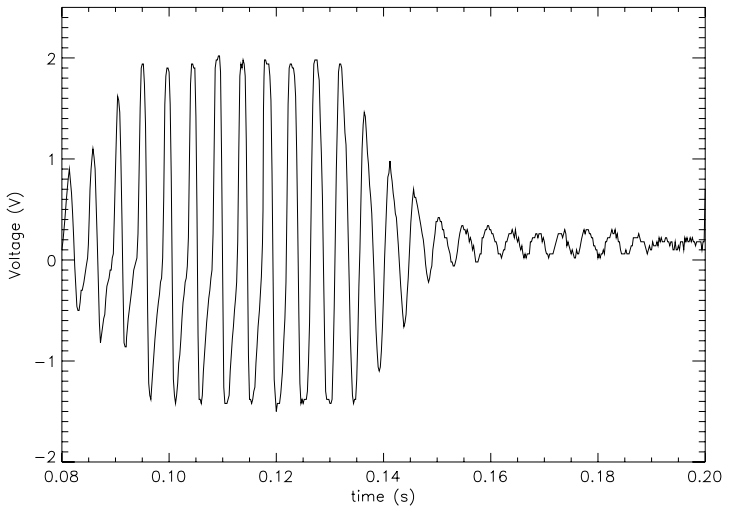

Figure 9: Doppler burst obtained from a calibration flow using a humidifier.

pedestal spectrum from the Doppler spectrum. A more detailed description of frequency shifting is given in the references cited at the beginning of this section; The von Karman Institute Proceedings (see bibliography) are particularly recommended. Fortunately, in the present experiment, the expected Doppler frequencies were sufficiently higher than the pedestal frequencies, that simple electronic filtering was sufficient.

Figure 10 is a diagram of the signal processing circuit used in the present work. The PM signal is either amplified or attenuated, depending on the signal level; low–pass filtered to get rid of the high frequency electrical noise; and high–pass filtered to eliminate the Doppler pedestal. The conditioned, filtered signal is fed into a Schmitt trigger where the signal is digitized and sent to a timing circuit. Two successive 200 mV pulses are required to start the count registers. Low and high count registers time the next 5 and 8 pulses respectively. This corresponds to measuring the time it takes for a particle to cross 5 and 8 interference fringes. It is expected that over such a short distance, the particle velocity would be approximately constant. A validation circuit compares the time measured by the low count register to 5/8 the time measured by the high count register. If the two registers are consistent to within a user–chosen tolerance, then the burst is validated; otherwise the burst is rejected. The entire validation process requires 10 fringes, two to start the count registers and eight to measure the frequency. This sets an inherent limit on the resolution of the system.

A Digital–Analog Converter (DAC) is part of the counter–processor unit. When a burst is validated, the DAC outputs a voltage proportional to the Doppler frequency of the burst; the proportionality constant is determined by a gain factor set by the user:

$$f_D(MHz) = \frac{100}{2^A} V_{DAC}(Volts) \tag{25}$$

where A is the DAC gain setting. If a burst is rejected, the DAC outputs its previous voltage. A digital readout gives the data rate and the number of bursts validated per 1000 bursts. These features are not relevant to a transient flow such as our experiment but were useful in calibrating the system. The filtered PM signal and the DAC output were monitored with a Tektronix 460A Digital Storage Oscilloscope capable of storing up to 120000 points.

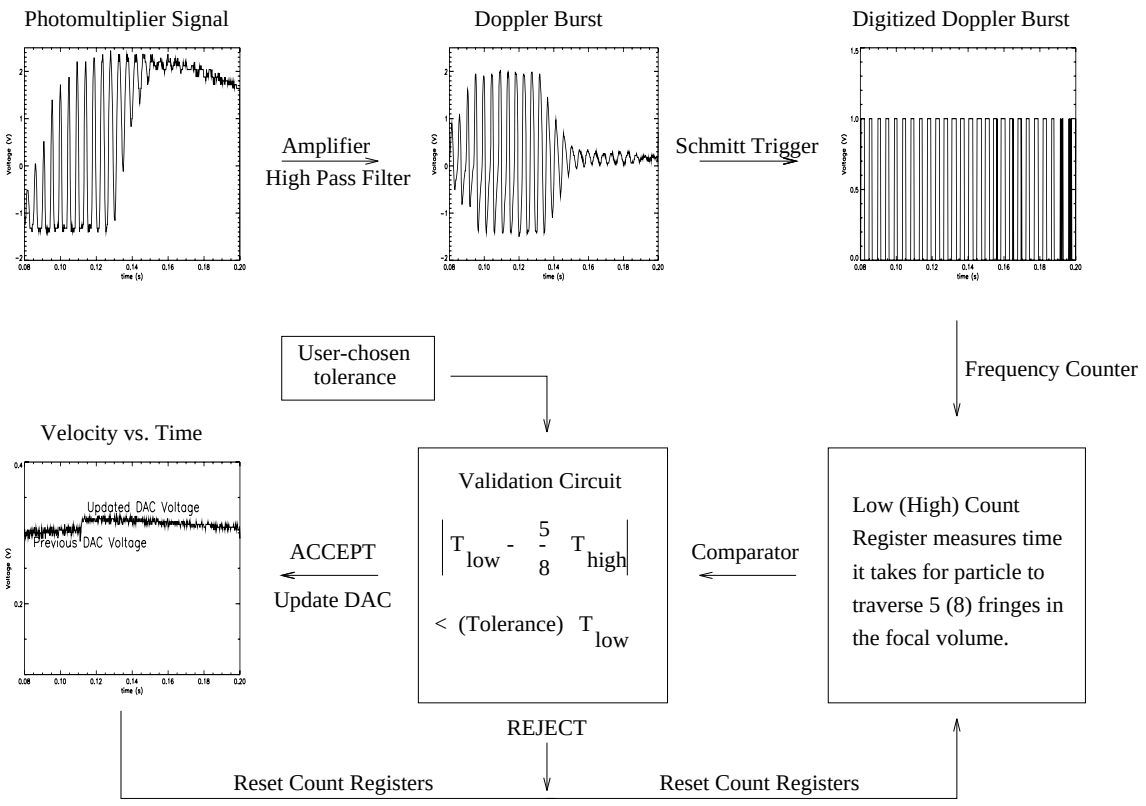

Figure 10: The signal processing circuit.

An important issue in LDV is seeding particles. Too few particles results in insufficient signal level. Figure 11 shows a situation with too many particles. Two bursts are merged into one signal

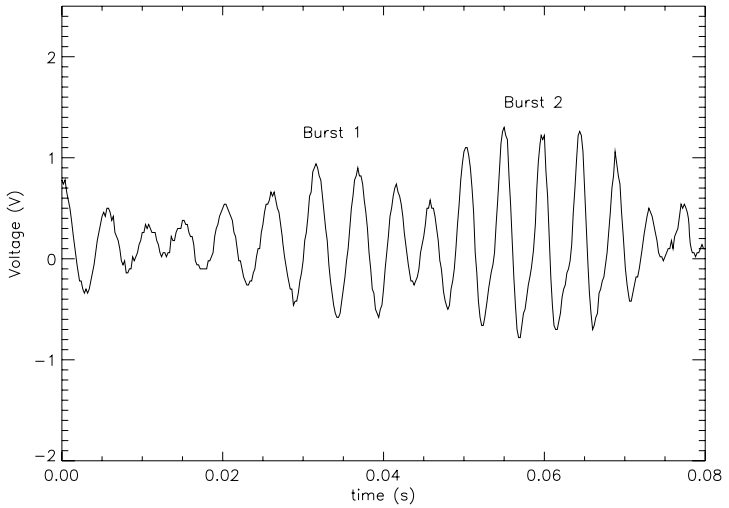

Figure 11: Two particles in the focal volume at the same time.

indicating that two particles passed through the focal volume at nearly the same time. This could potentially lead to a poor data rate as the counter would interpret the two bursts as a single burst.

In the figure shown, the two particles moved at nearly the same velocity so that the misinterpreting by the counter does not effect the measurement. However, one could imagine a situation where this would be important (i.e. in turbulent or quickly fluctuating flows). To determine the optimum seeding density for a flow, the seeding density should be varied and the filtered output of the PMT observed on an oscilloscope. The data rate and validation indicators on the counter are also useful for this purpose.

A final comment needs to be made on the interpretation of LDV as the detection of light scattered by a particle as it passes through a line of interference fringes. This is a very intuitive and useful way of looking at LDV but is not completely correct. A *beam* is a group of waves propagating through space at the same frequency. Each of the Ar–ion laser beams is composed of several blue and green beams and the average frequency of the Ar–ion beam is on the order of 10^{14} Hz. Measuring a particle velocity by directly measuring the Doppler shift of a laser beam scattered off the particle is unsuitable because the beam's frequency will be shifted only one part in 10^8. Consider the frequency spectrum in the region where two beams of equal frequency are made to cross. The two frequencies present in the focal volume are the difference frequency 0 Hz, and the sum frequency. What the PMT actually detects is the Doppler shift of the light scattered by a particle moving through the focal volume. However, the PMT is not fast enough to detect the Doppler–shifted sum frequency but only the Doppler–shifted difference frequency so only the latter is detected. The Doppler–shifted sum frequency appears only as a DC offset which contributes to the Doppler pedestal (with beams of nearly equal power, this may be the major component of the pedestal). The scattered fringe model of LDV gives no mention of the sum frequency so is not a complete description of the detection process. That the fringe model works is a consequence of the photomultiplier not being fast enough to detect the sum frequency. Exploiting the speed limitation of the photodetector is the idea behind heterodyne detection systems (such as this one) and is described in greater detail in Yariv (1997).

3 Experimental Procedure

The advantage of using the 4-beam He/Ne photodiode system to measure V_f is that the system is easily interfaced with the LDV for a simultaneous measurement of V_f and u_u. Because the photodiode system failed, the schlieren measurements were necessary. The schlieren measurements were performed one week after the LDV measurements.

3.1 Flow Velocity Measurement

The experimental procedure involved opening all valves to MCV and evacuating the system using the Sargent-Welch pump. The filling pressure was monitored using the Kulite pressure transducer connected to the NIDAQ–LabView system. When the reading on the pressure gauge would stabilize, the pressure transducer would be zeroed. Any drift in the zero reading in subsequent measurements was recorded as a zero offset.

After evacuation of the vessel and calibration of the pressure transducer, all lines to MCV were closed except the gas line going through the particle chamber. The flow control needle valve was set to 1/2–turn and the vessel was filled with air to 10–15 kPa. Then the air line was closed and the mixer turned on. There was now a seeded flow in the vessel. The PM optics were adjusted so that the collecting lens was focused on the LDV measurement location. The filtered PM signal

and the DAC output were checked on an oscilloscope to determine if there were enough seeding particles and if the Doppler bursts were validating.

If the LDV was working properly, the seeding chamber was bypassed and the vessel was filled to the desired concentration of air. Then the vessel was closed off fully and the gas lines were evacuated. After 20 seconds or so, the vacuum valve was closed and the fill lines were purged with hydrogen for about 10 seconds. Then one of the fill lines to the vessel was opened and the vessel was slowly filled to the desired partial pressure of hydrogen; then the vessel was closed off and the gases were mixed for about 60–90 s. The accuracy of this method of filling (often referred to as the method of partial pressures) was established by Pfahl and Shepherd (1997). Most of the runs were done with a final vessel pressure of 100 kPa (after the zero offset had been subtracted off; the zero offset was typically 0.1-0.7 kPa). The hydrogen in the lines was diluted with nitrogen and pumped out through the exhaust system; the mixer was turned off; and the flow in the vessel was allowed to decay.

The scope trigger was set at 1.8V; the scope was set to single acquisition mode; the TM–11A was armed; and the data acquisition system was armed. The trigger level was chosen so that the only pulse that could trigger the scope was the TM–11A firing signal. The mixture was ignited. After the combustion products had cooled off, the final temperature and pressure were noted. If the mixture had burned, the waste products were exhausted through the vacuum line.

3.2 Flame Speed Measurement

The procedure with the schlieren experiments was similar in terms of the filling except that the particle chamber was not used. Before each run, the run counter on the CCD had to be updated. Immediately before firing, the VCR record button was pressed.

4 Experimental Results

4.1 Test Conditions

The LDV data were taken one week before the schlieren data. Four LDV experiments were performed for each H_2 concentration between 10% and 5%. One day after these experiments, 14 more experiments were done at concentrations less than 5%; these concentrations ranged from 4.2% to 4.8%. It should be noted that a run at 9.8% may be counted among the 10% runs as often there were small variations ($\pm 0.2\%$) in the actual H_2 concentration.

One schlieren experiment was performed for each concentration from 10% to 5%. In addition, three schlieren experiments were done at concentrations less than 5% (4.3%, 4.6%, and 4.7%). The distance between the spark gap and the top of the flame as a function of time was obtained from each schlieren movie using an Epix frame grabber and image analysis system. The apparent flame speed, V_f, as a function of time was obtained by numerically differentiating the distance–time data using a three–point Lagrangian interpolation routine contained in the PV–WAVE data analysis package. For fuel concentrations lower than the downward flammability limit of 8%, the distance between the spark gap and the bottom of the flame as a function of time was also measured.

$V_f(t)$ is the apparent flame speed as viewed in the lab frame while $u_u(t)$ is the fluid velocity at the LDV measurement location as a function of time. The difference, $S_u(t) = V_f(t) - u_u(t)$,

can be interpreted as a burning velocity only at the time corresponding to the flame reaching the LDV measurement location. As the flame propagates from the spark gap to the LDV measurement location, it pushes the unburned fluid in front of it due to the volume displacement caused by the lower density of the burned gas relative to the unburned gas. We would expect the velocity measured at the LDV measurement location to increase as the flame approaches due to this piston–effect and the spherical geometry of the problem. This is evident by considering a steady point source at the origin in an infinite volume vessel assuming incompressible flow (see Fig.12).

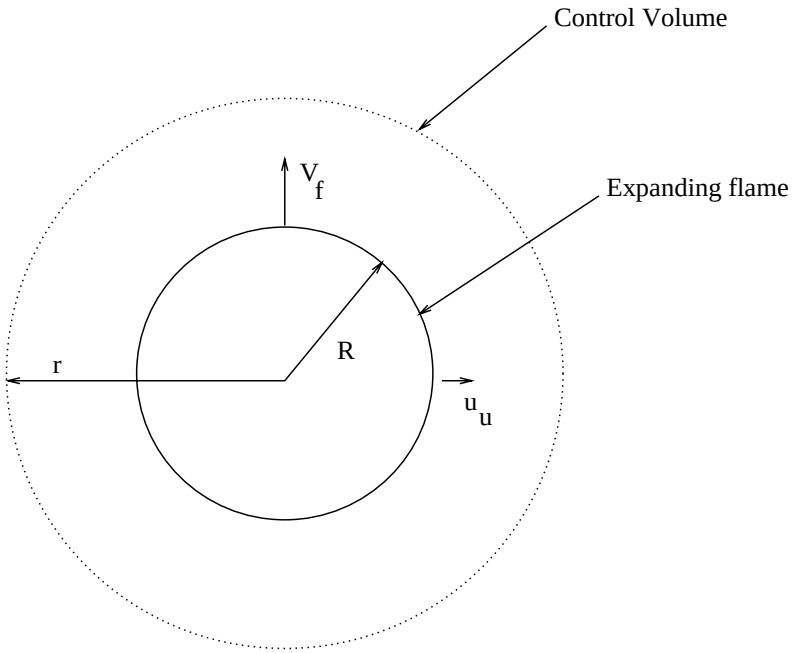

Figure 12: Point source model of an expanding flame.

The infinite volume assumption is valid for the initial expansion when the vessel wall effects are negligible. Incompressible flow is reasonable in the burned and unburned regions separately (but obviously not valid across the flame) due to the low Mach number of the flow. Also, we are ignoring buoyancy and other flame acceleration effects (i.e., assume that V_f is constant). Ignoring buoyancy is justified for concentrations significantly above the downward flammability limit (see LDV and Schlieren Data) but is not a valid approximation for the flames investigated in this study with the exception of the 10% H_2 flame. However, this oversimplified model of the expanding flame does illustrate why one would expect the velocity at the LDV measurement location to increase as the flame approaches. Defining t=0 as the time of the spark, the radial position of the flame at time t is

$$R(t) = V_f t \tag{26}$$

corresponding to a time rate of change of burned mass of

$$\frac{dM}{dt} = 4\pi R^2 \rho_b V_f \tag{27}$$

Continuity across the flame (assuming stationary products) implies:

$$\rho_u S_u = \rho_b V_f \tag{28}$$

Combining Eqs. 27 and 28 using Eq. 3 with $u_b = 0$ gives:

$$\frac{dM}{dt} = 4\pi R^2 \rho_u (1 - \frac{\rho_b}{\rho_u}) V_f \tag{29}$$

However, incompressible flow implies that the mass flux through a surface of radius r centered on the source must be the same for any r implying:

$$\frac{dM}{dt} = 4\pi r^2 \rho_u u(r) \quad r \geq R \tag{30}$$

Equating Eqs. 29 and 30 and using Eq. 26 gives the fluid velocity as a function of time at some distance r from the spark gap upstream of the flame.

$$u(r,t) = \frac{(1 - \frac{\rho_b}{\rho_u}) V_f^3 t^2}{r^2} \quad r \geq R \tag{31}$$

Our simple model predicts a velocity rise as the flame approaches that is quadratic in time and illustrates the effect of the spherical geometry; note that for a cylindrical geometry, our model would predict that u_u is linear in time while for a planar geometry, u_u is constant as the flame approaches. Figure 14 shows u_u versus time at a "fixed" measurement location for the 10% case and it is observed that the velocity rises with an approximately parabolic shape (the reason for the quotation marks will be discussed below).

The finite volume of MCV implies that the unburned gas would be compressed as it is displaced by burned gas. This causes the pressure in the vessel to rise significantly after a substantial fraction of the mixture has reacted. However, during the brief interval of interest to the velocity measurement, the vessel pressure is essentially constant. The pressure trace in Fig.14 gives experimental verification of this statement. It should be noted that due to this finite volume effect, a large vessel is expected to yield more accurate measurements of S_u than a smaller vessel.

So the fluid velocity at the measurement location rises quadratically in time as the flame approaches the measurement location. As the flame passes by the measurement location, we would expect a sudden decrease in the fluid velocity, given by Eq. 3. A sharp drop in the LDV velocity trace is expected at the instant the flame reaches the LDV measurement location. A flame speed is calculated by interpolating the flame velocity–time data from the schlieren measurements at the arrival time marked by the LDV drop. The fluid velocity immediately prior to the LDV drop is subtracted from this interpolated flame speed to give the burning velocity S_u.

At 10% fuel concentration (see Fig. 14), we can clearly observe the expected drop behavior. At 9% fuel concentration (see Fig. 15), the drop is distinguishable but less pronounced. At 8% fuel concentration (see Fig. 19) and lower, the drop is no longer apparent. To facilitate finding the time when the flame reached the LDV measurement location, three nominal flame arrival times were determined by interpolating the flame position–time data at three positions. The first position was the distance between the spark gap and the LDV measurement location with no flame. The second position was determined by interpolating the 10% H_2 flame position–time data at the time corresponding to the 10% H_2 LDV drop. The third position was an average of the two.

The first position was insufficient by itself because beam steering (shifting of the LDV probe location due to the changing index of refraction as the flame approaches) was neglected. The second position was insufficient because the effects of beam steering were overestimated. Beam steering would be a greater effect in the 10% flame than the 8% flame due to the increased amount of combustion and the cellular instability. The third position was a compromise being an average of the two.

4.2 LDV and Schlieren Data

The data for selected runs are shown in Figs. 13 through 19.

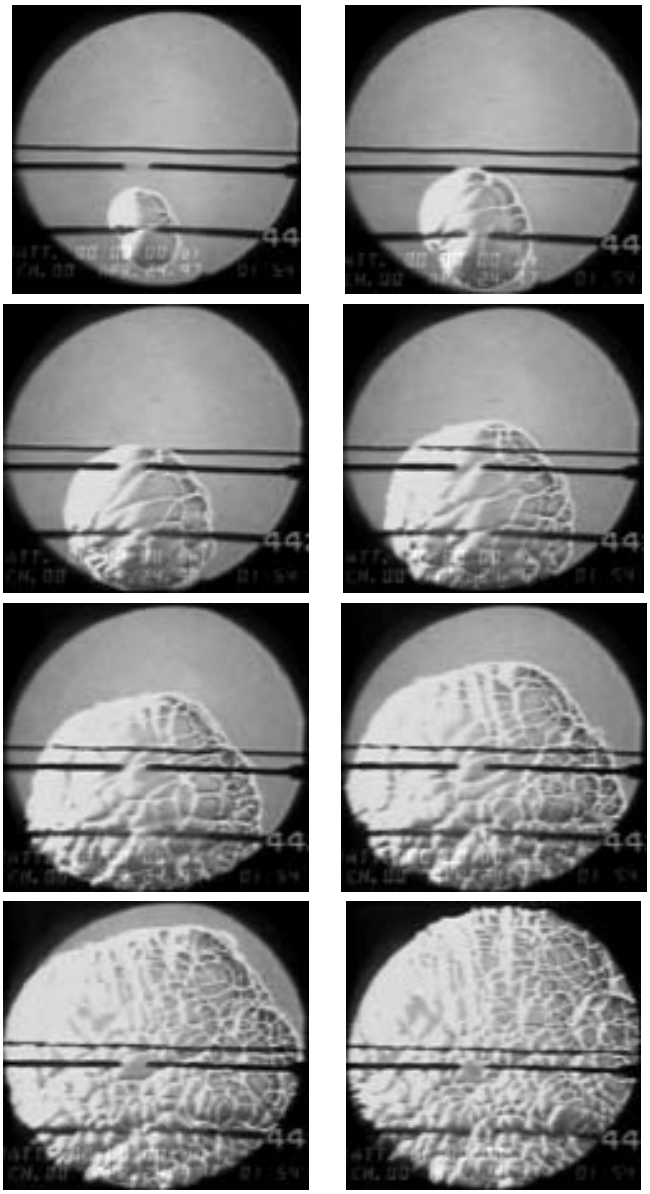

Figure 13: Selected frames from the schlieren video for Experiment 442, 10% H_2 concentration.

The most reliable data for this experiment is for 10% H_2 concentration (see Figs. 13 and 14). Figure 13 is a sequence of schlieren video frames separated by 17 ms. The lower pair of electrodes are MCV's feedthrough spark electrodes discussed earlier while the upper pair of electrodes belong to the CONVOL 400 ℓ facility; the windows of the two test vessels were lined up during the experiments. The horizontal line across the field of view is a wire tied to the outside of the window port marking the vertical position of the LDV measurement location with no flame. Wrinkles in the flame surface are observed as early as the second frame. This deformation of the flame surface is called *cellular instability*. Another noticeable feature is that the bottom of the flame kernel is not

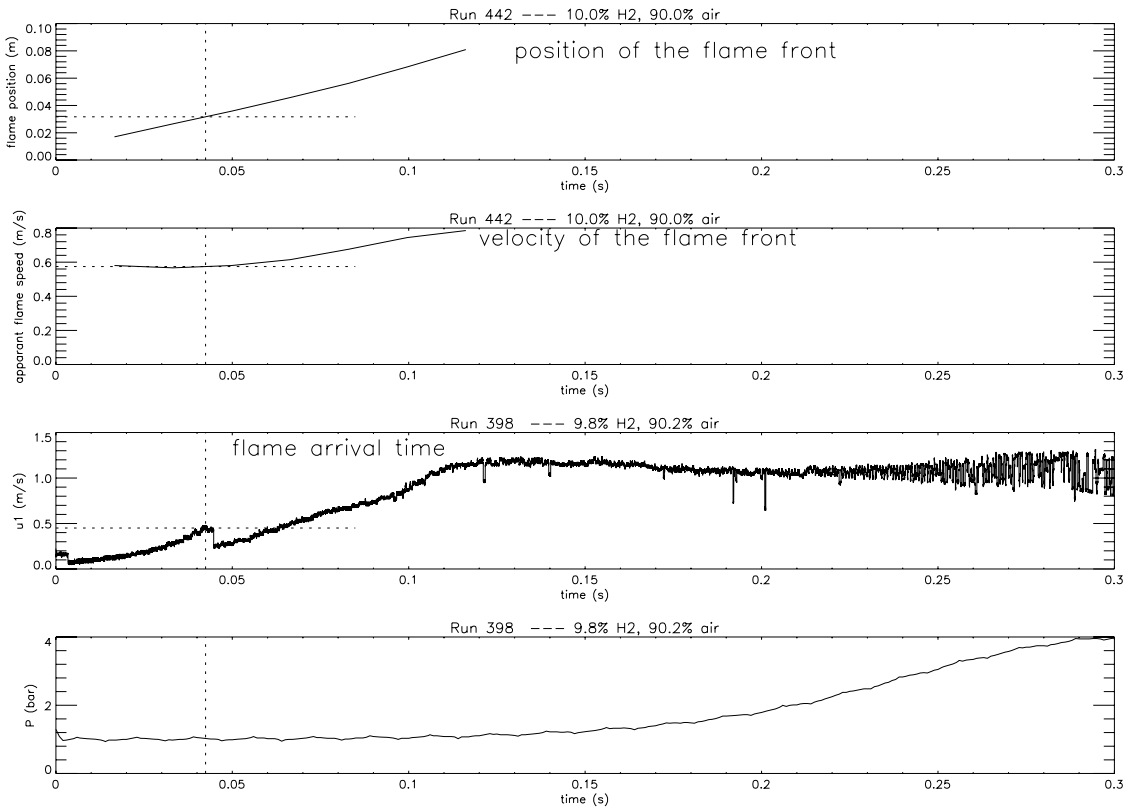

Figure 14: Flame position and LDV data for Runs 398 and 442 at 10% H_2.

visible in the photographs. Buoyancy causes the flame to rise while combustion causes the flame to expand radially. At the top of the flame, these two forces are in the same direction and it is clear from the photographs that the top of the flame front rises with time. At the bottom of the flame, these two forces are in opposite directions. The photographs imply that the burning velocity of a 10% H_2-air flame is higher than the velocity induced by buoyancy so the bottom of the flame propagates downward with time.

Figure 14 displays the schlieren and LDV information plotted versus time. It should be emphasized that the LDV measurement is not exactly the velocity trace at a fixed location due to beam steering effects. However, the clear discontinuity near t=40 ms can be interpreted as the time the flame arrived at the LDV location, wherever that location may have been. From this arrival time, the flame position curve, flame velocity curve, and LDV trace can be interpolated to determine the LDV measurement location, V_f, and u_u.

The burning velocity S_u is a function of initial conditions (reactant temperature, pressure, and composition) and is independent of position. This implies that if V_f and u_u are known at the same time and position, the difference $V_f - u_u$ can be interpreted as the burning velocity of the mixture even if the position is not known exactly. In other words,

$$V_f(x, t_{arrival}) - u_u(x, t_{arrival}) = S_u \tag{32}$$

for any x. This explains the choice of $R(t)$ in Fig. 6 as the top of the flame is the part of the flame that passes through the LDV measurement location. Therefore, $R(t_{arrival})$ is the LDV

measurement location when the flame arrives so that $\frac{dR}{dt}(t_{arrival})$ would be the proper flame speed to use in calculating S_u.

Some features of the LDV trace in Fig. 14 deserve comment. The sudden discontinuity near t=0 s is unphysical; it is just the DAC updating from the previous run. The five spikes in between t=0.1 s and t=0.2 s are also unphysical. The DAC's maximum output is 1.25 V so when it is forced to output more, it drops out as observed. The velocity rise after the flame passes the measurement location is due to the compression effect caused by the finite-volume of the vessel. In an infinite volume vessel, the burned fluid velocity would stay near zero. The oscillations setting in at t=0.2 s are due to the turbulent flow associated with the flame reaching the top of the vessel.

The schlieren photographs for 9% H_2 were similar to the 10% photographs in that the bottom of the flame was not visible. Cellular instabilities could not be seen in the movie so it was inferred that the onset of cellular instability occurs between 9% and 10% H_2. Figure 15 shows the schlieren and LDV data from the 9% experiment. The velocity drop in the LDV trace is apparent but less pronounced than in the 10% case.

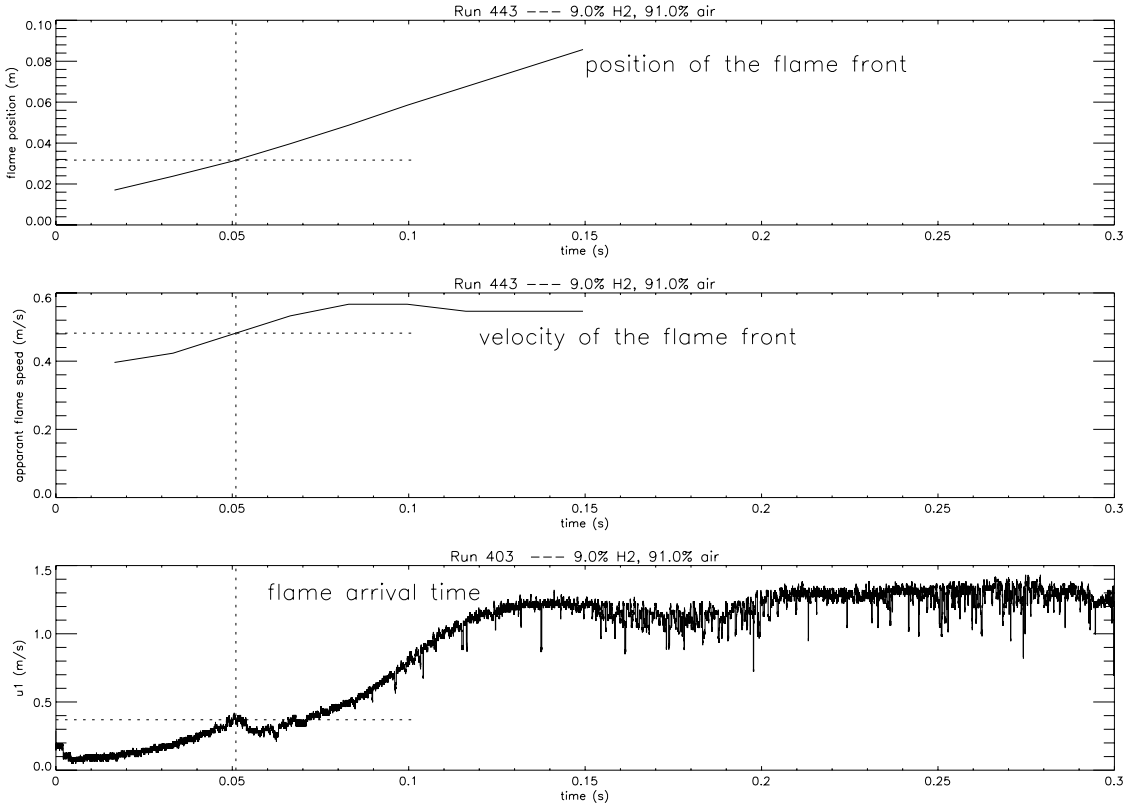

Figure 15: Flame position and LDV data for Runs 403 and 443 at 9% H_2.

At 8% H_2, the qualitative behavior of the flame changes significantly. Figure 16 is a plot of peak pressure, measured by a pressure transducer on a side wall of the vessel, versus concentration for the mixtures investigated in this experiment. The peak pressure changes drastically between 8 and 9% H_2; this is due to the onset of downward combustion, documented in all previous studies of hydrogen-air flammability. These measured peak pressures correlate well with the adiabatic explosion pressures given in table 3 in the 9% and 10% cases but are quite lower than the theoretical values for the 8% and lower cases. This is a finite volume effect as the 8% flame quenches before

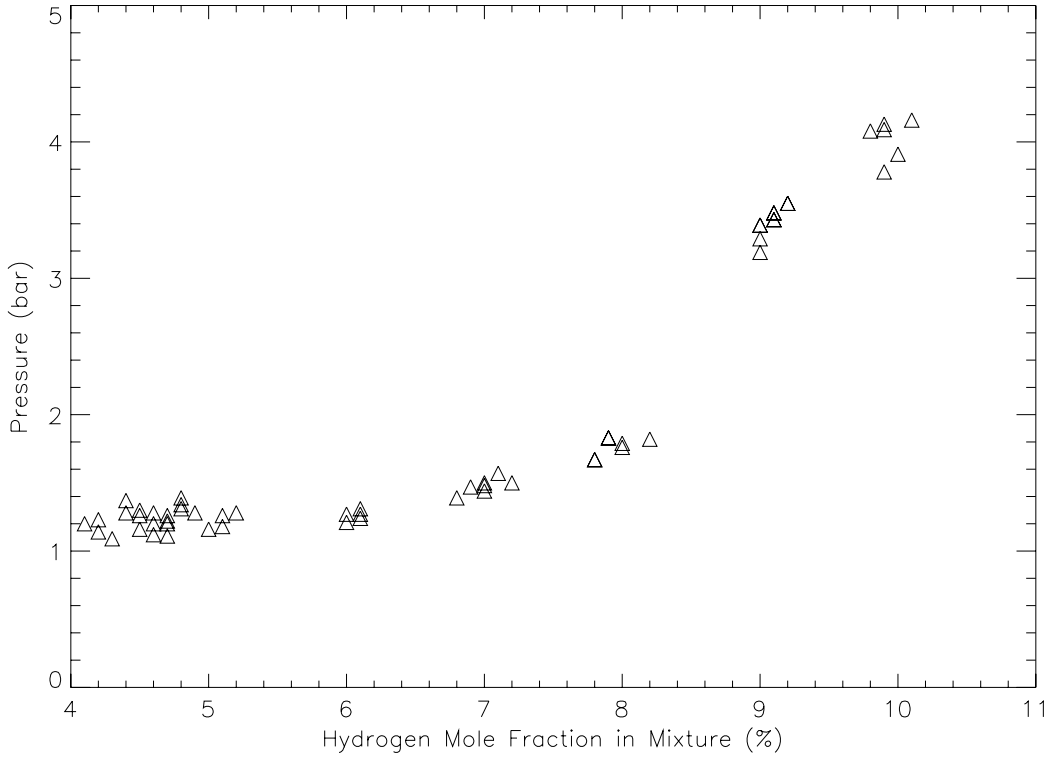

Figure 16: Peak pressure vs. hydrogen molar concentration.

the kernel can fill the vessel. This will be discussed more below. Figure 17 is a sequence of schlieren video frames separated by 68 ms (i.e. every fourth frame of the schlieren movie). The bottom of the flame is visible for the first time implying that the velocity induced by buoyancy is larger than the burning velocity. This indicates that the downward flammability limit for H_2-air mixtures is between 8 and 9% H_2 (Coward and Jones 1952). The downward flammability limit of a combustible mixture is the leanest composition for which the flame will propagate downwards. In other words, the downward flammability limit of a combustible mixture is the leanest composition for which the burning velocity is greater than the velocity induced by buoyancy.

The transition to downward propagation occurring between 8 and 9% explains the drop in the peak pressure vs. concentration curve in the same interval. Simple 1–D flame analysis showed that the pressure is approximately constant across a laminar flame. However, this was for an infinite volume vessel. In a finite volume situation, the burned gas displaces an equal volume of higher density unburned gas causing the unburned gas to be compressed, e.g. its density rises. This compression is nearly adiabatic (Andrews and Bradley 1972) and causes the pressure inside the vessel to increase substantially after a significant fraction of the mixture has burned. The 9 and 10% flames would displace a large volume of unburned gas before quenching on the walls (e.g. the flame would expand and quench on the walls). However, the 8% flame quenches before it gets the opportunity to displace a substantial volume of unburned gas because the flame rises and quenches on the top of the vessel before expanding a significant amount. This explains why the (side wall) peak pressures of 9 and 10% mixtures are nearly twice as high as with 8% mixtures. This argument implies that in a microgravity experiment, the peak pressures of 8 and 9% mixtures would be closer

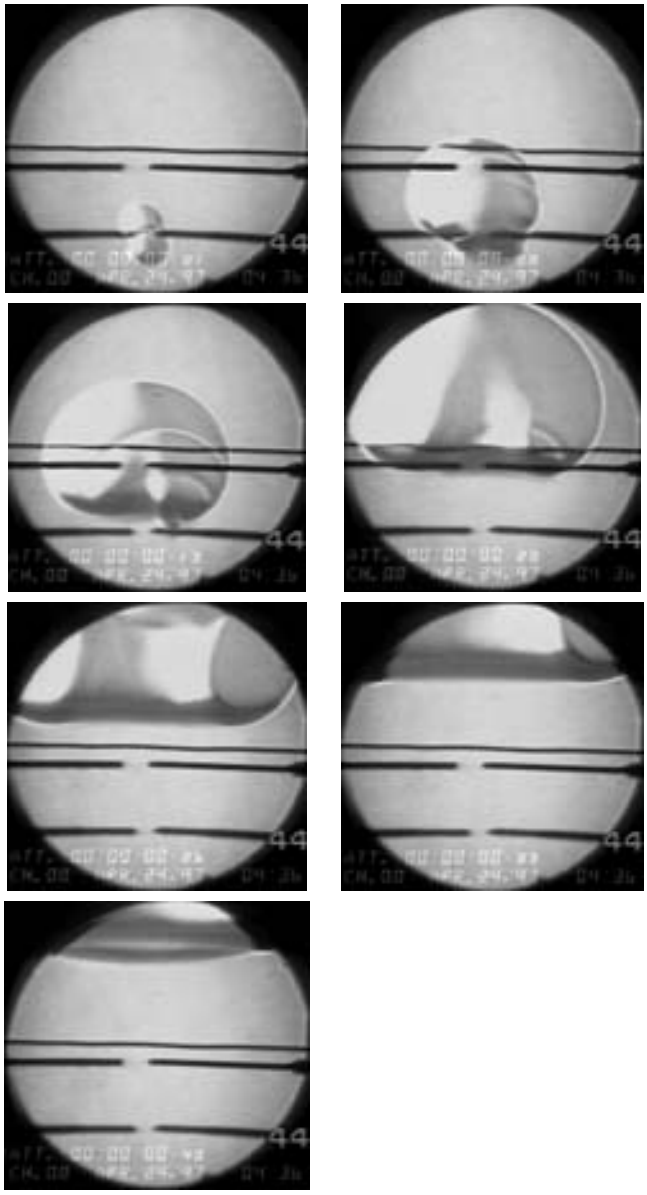

Figure 17: Selected frames from the schlieren video for Experiment 444, 8% H_2.

in value although the 9% pressure (versus time) trace would peak before the 8% pressure trace due to the higher burning velocity of the 9% mixture.

The lowest curve in Fig. 14 is a plot of pressure versus time measured at a side wall of MCV by the Kulite transducer. It is noted that though the pressure rise due to compression begins at around 0.15 s, the pressure is essentially constant during the measurement interval of interest. This validates the use of the constant pressure assumption in the present work and the Ross study. Only the 10% pressure trace has been included but it is clear that the constant pressure assumption is also valid at leaner concentrations since the compression effects would be less than in the 10% case.

The deformation of the flame front as the flame rises is quite interesting. The top of the flame keeps its spherical shape while the bottom of the flame seems to be "pinching" inward near the

center. This "pinching" is quite clear in the last frame of the movie. A possible reason for this effect is that the upward component of the burned fluid velocity u_b may be greater near the center of the flame due to vorticity generated by the misalignment of the density and pressure gradients caused by the gravitational field. This is depicted in Fig. 18.

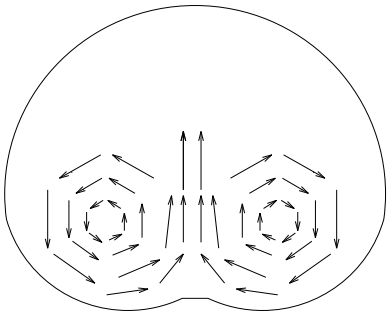

Figure 18: Vortex pair caused by the gravitational field.

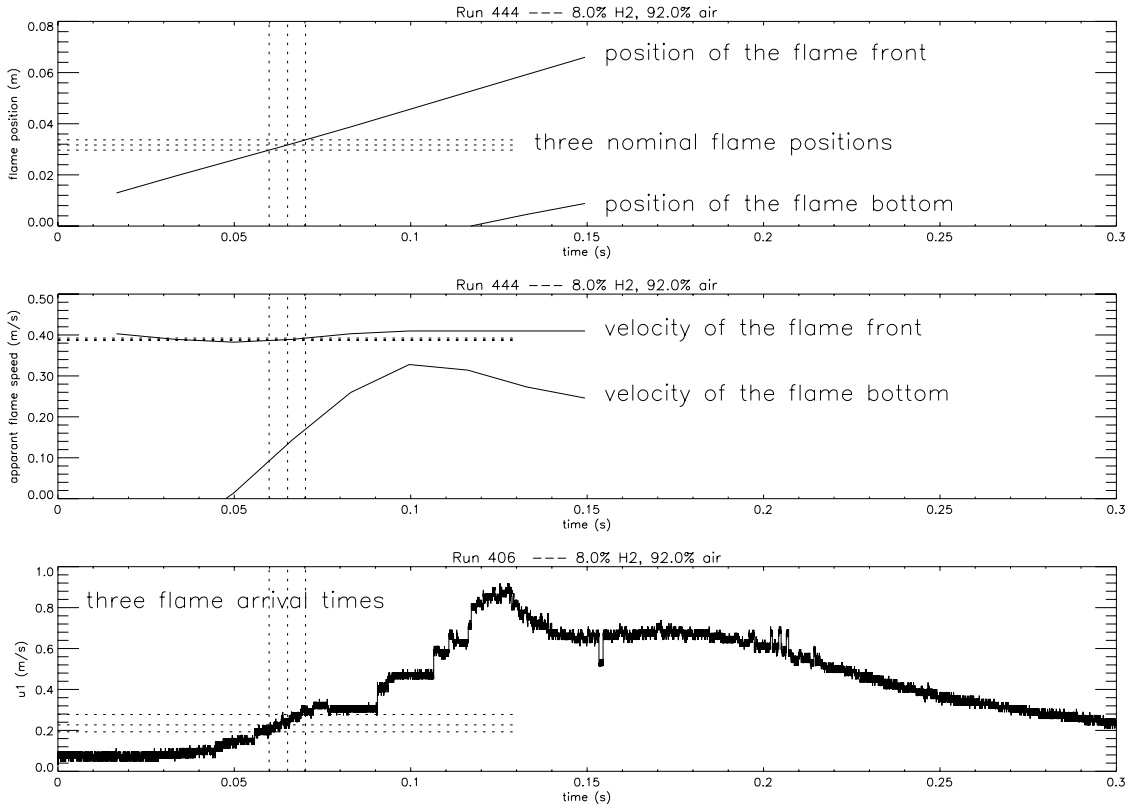

Figure 19: Flame position and LDV data for Runs 406 and 444 at 8% H_2.

Figure 19 shows the schlieren and LDV data for the 8% experiments. The LDV traces were surprisingly reproducible but a clear velocity drop was not observed as in the 9 and 10% runs. In all three 8% experiments, a sharp downward slope was observed near t=0.125 s. The cause of this feature is unclear but it was determined that neither the top or bottom of the flame passing the LDV location was the cause. The top of the flame would pass by in the time interval spanned by the three estimated flame arrival times. The bottom of the flame passing by would cause a velocity

jump, not a velocity drop.

The absence of a velocity drop to mark the flame front necessitated the use of the three nominal flame positions to interpolate the three flame arrival times as discussed in an earlier section. Using values for S_u determined from this study and Ross (1996), a value for the density gradient ρ_u/ρ_b obtained from Ross, and Eq. 3, it was estimated that the velocity drop for 8% H_2 should be between 12 and 15 cm/s. The one–bit noise is around 5 cm/s so the jump would have been quite small had it been observed on the velocity trace. In contrast, the jump for 9% H_2 should be between 22 and 26 cm/s and therefore, much more apparent relative to the one–bit noise. The jump for 10% H_2 would be larger still. It is possible that the flame arrived immediately after the three passage times when the DAC signal suddenly went flat before rising again. A sudden dropout is unlikely so it is possible that insufficient DAC gain was the problem. Perhaps the flat DAC signal is a consequence of the actual velocity jump being too small to distinguish under the DAC gain used. It is worth redoing the experiments with higher DAC gain to see if this indeed was the problem.

At concentrations leaner than 8%, the same problem of being unable to determine the flame passage time was encountered. Insufficient gain was definitely a factor in these measurements as the one–bit noise became larger than the expected velocity drop. The schlieren films for these concentrations showed similar qualitative behavior as 8%. The leanest concentration investigated was 4.2% H_2.

At some of the very lean concentrations, the error is quite high because the flame speed and unburned fluid velocity were nearly equal, the difference being a very small number. This is expected as the burning velocity would be quite small near the flammability limit. Guesswork was required to determine a reasonable flame arrival time at which to measure the burning velocity. Within the range defined by the three estimated flame arrival times, there would sometimes be values of $t_{arrival}$ where $V_f - u_u$ was negative or too large. The knowledge that S_u is monotonic with concentration for lean mixtures was used in determining a suitable $t_{arrival}$. For instance, when investigating the data for a 5% H_2 mixture, times where $V_f - u_u$ was greater than the burning velocity for 10% H_2 were discarded as being possible candidates for $t_{arrival}$. The obvious problem of this method is the subjective component of deciding what is a "suitable" data point. The best solution would be to optimize the LDV system parameters for concentrations less than 8% H_2 and redo the measurements. Increasing the DAC gain would be a first step.

5 Discussion of Results

A plot of S_u versus H_2 concentration is given in Fig. 20 along with results from other investigations. The large error bars at the leaner concentrations is indicative of the uncertainty inherent in the flame arrival time estimation methods used. Still, the results are of the same order of magnitude as previous measurements made in normal gravity although there are not many data points to compare with.

For 8-10% H_2, the values for S_u obtained in the present work are scattered throughout the range defined by the previous works of Ross, Koroll et. al., and Egolfopoulos and Law. At leaner concentrations, the present work correlates well with the two data points of Ross which was the only normal gravity study obtaining such measurements.

Of more interest is the wide discrepancy between this experiment and the results of Ronney. The two primary differences in test conditions are the microgravity conditions of Ronney's experiment

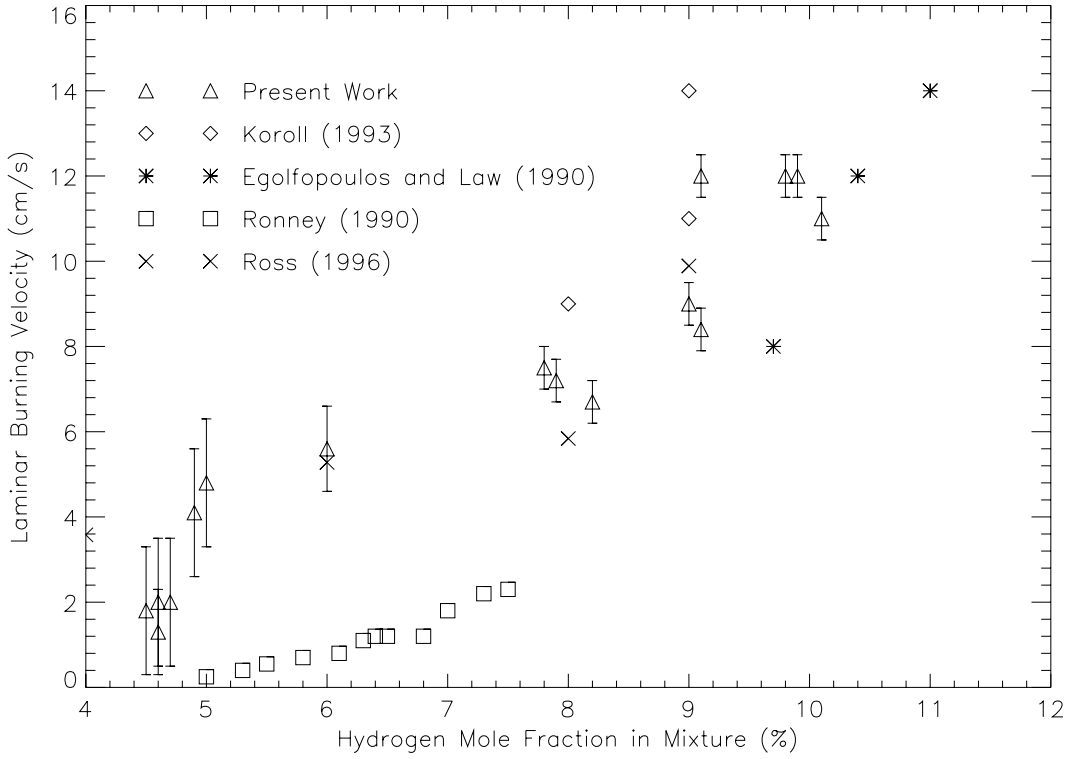

Figure 20: S_u vs. H_2 concentration near the lean flammability limit.

versus the normal gravity conditions of the present work; and Ronney's use of a combustion inhibitor CF_3Br to help visualize the flame. Both of these differences would produce the observed trend that the present experiment's results (and Ross's results) are substantially higher than Ronney's. The effects of the inhibitor and the effects of buoyancy need to be quantified. The large error bars on the leaner velocities in the present experiment need to be considered as well.

Westbrook (1983) observed in a numerical study that using 1% CF_3Br decreased the burning velocity of a stoichiometric H_2-air mixture at atmospheric pressure by 23%. Ronney observed that for a 7% H_2 flame, 0.4% inhibitor decreased the burning velocity by 27%. Ronney noted that the qualitative behavior of the flames were unchanged by the inhibitor. The inhibitor seemed to act primarily by "increasing the impact of heat loss through the increase in the concentration of strongly radiant combustion products" (Ronney 1990).

Buoyancy affects the measurement of burning velocity through the distortion of the flame surface through the advection of the flame by buoyancy-induced flow. This distortion can be visualized as "stretching" of a hypothetical flame surface. Flame stretch is a key factor (Law 1988) in flame dynamics. Models of flame structure predict and measurements demonstrate a dependence of laminar burning velocity on stretch factor K

$$K = \frac{1}{A}\frac{dA}{dt} \tag{33}$$

where A is a representative element of the flame surface area (see Figure 21). Both the curvature of a propagating flame and gradients or *strain* in the flow contribute to the stretch factor.

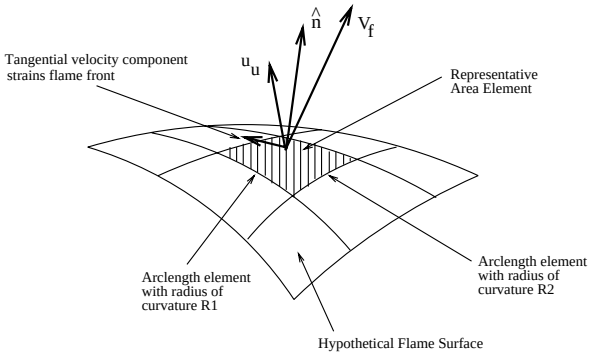

Figure 21: A representative area element of a hypothetical flame surface.

Theoretical models (Matalon (1983)) predict that for low Lewis number flames (which include the lean hydrogen flames studied in the present work), positive stretching will increase the burning velocity and negative stretch will decrease it. If the magnitude of the stretching is too large, extinction of the flame can occur, as discussed by Giovangigli and Smooke (1987). Any experimental measurement of flame speed involves a flow configuration that creates stretch either associated with the motion of the flame or gradients in the upstream flow. Therefore to some extent, all measurements of burning velocity are contaminated by flame stretch. In most previous experiments, the effects of flame stretch were not quantified and this results in some uncertainty in the reported values of burning velocity. Recent measurements of flame speed have recognized the effects of stretch. For example, Egolfopoulos and Law (1990) measure burning velocity in a stagnation point flow as a function of strain and extrapolate to zero strain.

The amount of stretching can be estimated for the present configuration by considering a simple model of the flow field produced by a radially-expanding, rising flame. Figure 22 shows computed trajectories of several fluid elements approaching the top of the flame, as viewed in coordinates moving with the flame front. These trajectories are based on a simple model of the flow developed later in this section. The flame surface is curved and the flow is diverging in the reactants as they approach the top of the flame. As the flame surface is crossed, the streaklines deflect inwards due to continuity. This figure assumes that the fluid elements move with constant velocity inside the flame kernel.

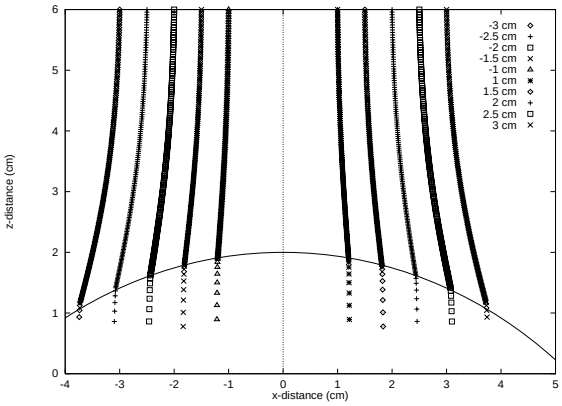

Figure 22: Trajectories of representative fluid elements passing through the flame surface. The flame curvature and upward motion causes the flow in the reactants to diverge as the flame is approached. Continuity causes the streaklines to deflect inwards after passing through the flame.

Figure 23 illustrates the geometry associated with the streakline deflection across the flame. The logic associated with the construction of this figure is given by the velocity relationships and the conservation laws as approximated for low-speed flame fronts. These relationships are:

$$w_u \equiv V_f - u_u \tag{34}$$

$$w_b \equiv V_f - u_b \tag{35}$$

$$u_u > u_b \rightarrow w_u < w_b \tag{36}$$

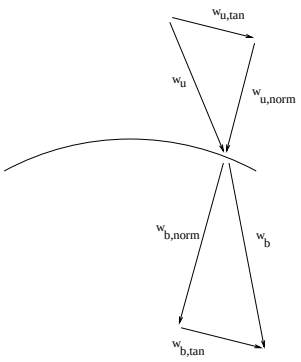

Figure 23: Streakline deflection across an oblique flame front.

The specific flow being modelled in figure 22 is the 10% H_2 flame. Eight different fluid elements are followed, each trajectory being marked by its initial distance from the axis of the flame kernel. The initial height above the origin is 6 cm for all eight trajectories. The origin is the initial location of the center of the flame kernel. The reference frame is chosen so that the north pole of the flame kernel is fixed. The center of the flame kernel, which moves upward with velocity V_b in the lab frame, moves downward with velocity $V_f - V_b$ in this reference frame. The start time of the simulations corresponds to the time when the flame kernel is 2 cm in radius and each curve represents approximately 0.1 seconds, after which the kernel is approximately 7 cm in radius. After choosing a fluid element, i.e. selecting an initial (x,z) pair, the motion of the fluid element is mapped out using an iterative scheme where the velocity field is that developed later in this section. The scheme is stopped at the time when the fluid element reaches the flame front. The velocity inside the flame is assumed constant. Continuity gives the velocity in the z-direction while the x-component of the velocity is unchanged. Strictly, this is only true at the north pole but the approximation is reasonable on the top portion of the flame surface which is the region of interest.

The flame surface is drawn by first approximating the portions of the flame surface near the north pole of the flame kernel as being fixed in the z-direction. Once again, this is only exact at the north pole. The radius of curvature, R, of this top portion of the kernel and the location of the center of the kernel, z_0, are computed at the stop time of the simulation. The equation of the flame surface near the top of the flame is thus approximated as the equation of a circle of radius R centered at $z=z_0$.

Representative values for S_u and the density jump obtained in the present work are used in the computations. A value for the component of V_f due to buoyancy is determined by subtracting the V_f obtained in Ross's study, where gravity effects were estimated to be very small, from the V_f obtained through the schlieren measurements in the present work.

The stretch factor can be computed using the expression derived by Matalon (1983)

$$K = -\,\mathbf{n}\cdot\nabla\times(\mathbf{u}\times\mathbf{n})|_s + (\mathbf{V_f}\cdot\mathbf{n})(\nabla\cdot\mathbf{n})|_s \tag{37}$$

where the subscript s refers to the flame surface, $\mathbf{n}$ is the unit normal (directed into the reactants) to the flame surface, $\mathbf{u}$ is the flow velocity and $\mathbf{V_f}$ is the flame front velocity.

We can estimate the stretch K for the present experiment by using two simple potential flow models for the velocity field induced by the flame. First consider just the flow induced by an ideal radially-symmetric flame. This is the model considered earlier in Subsection 4.1 and summarized by Eq. 31. In vector notation, the velocity field outside the flame $r \geq R$ is

$$\mathbf{u} = U_R\frac{R^2}{r^2}\frac{\mathbf{r}}{r} \qquad U_R = \left(\frac{\rho_u}{\rho_b} - 1\right)S_u \tag{38}$$

We model buoyancy as giving the flame a velocity V_b in the upward direction. The velocity field produced by this motion will be modeled as incompressible potential flow over a sphere. If the surface of the sphere corresponds to the flame front, then the boundary conditions at the surface of the flame will be satisfied by superimposing the radial motion given by Eq. 38 with the motion associated with the flow over the sphere. For the purposes of the present computation, it is simplest to consider the sphere stationary (centered at the origin) and to allow the flow at infinity U to be equal in magnitude to V_b. If the coordinates are such that the top of the flame is located on the negative z-axis, at z = - R, then the sphere-flow velocity field is

$$\mathbf{u} = -\frac{R^3U}{2}\left(\frac{3z}{r^5}\mathbf{r} - \frac{\hat{\mathbf{z}}}{r^3}\right) + U\hat{\mathbf{z}} \tag{39}$$

Now consider evaluating the terms in Eq. 37. For flow produced by the radial expansion, $\mathbf{u}\times\mathbf{n}$ = 0, since the flow is radially outwards, and therefore the first term in Eq. 37 is zero. In general, the second term can be evaluated by observing that the divergence of the surface normal can be computed from the principal radii of curvature, R_1 and R_2.

$$\nabla\cdot\mathbf{n} = \frac{1}{R_1} + \frac{1}{R_2} \tag{40}$$

For a spherical flame, the two radii are equal and have the common value of the radius of the flame. In coordinates where the center of the flame is stationary, the flame velocity is equal to the radial expansion rate and in the direction of the surface normal

$$\mathbf{V_f} = \frac{dR}{dt}\mathbf{n} \tag{41}$$

Therefore the flame stretch factor for the radially-expanding, spherical flame is

$$K = \frac{2}{R}\frac{dR}{dt} \tag{42}$$

There is an additional contribution due to the straining motion in the flow induced by the moving sphere approximation used to model the upward motion of the buoyant flame ball. This motion only contributes through the first term in Eq. 37. The first term can be rewritten using a standard vector identity to yield:

$$\nabla\times(\mathbf{u}\times\mathbf{n}) = (\mathbf{n}\cdot\nabla)\mathbf{u} - (\mathbf{u}\cdot\nabla)\mathbf{n} - (\nabla\cdot\mathbf{u})\mathbf{n} + (\nabla\cdot\mathbf{n})\mathbf{u} \tag{43}$$

This expression can be considerably simplified by recognizing that we are evaluating the velocity field at a stagnation point (the top of the flame) where $\mathbf{u} = 0$. Also, the flowfield can be considered incompressible $\nabla \cdot \mathbf{u} = 0$. In this case, only one term from Eq. 43 is nonzero:

$$\mathbf{n} \cdot ((\mathbf{n} \cdot \nabla)\, \mathbf{u}) \tag{44}$$

Physically, this corresponds to the normal component of the velocity gradient in the direction normal to the flame front. Evaluating this for the sphere flow, we find that

$$K = \frac{3}{R} U \tag{45}$$

which can also be found by expanding the flowfield in the vicinity of the stagnation point. In axisymmetric flow, it is known that the flow near a stagnation point can be locally expressed as

$$\mathbf{u} = (\frac{K}{2}x, \frac{K}{2}y, -Kz) \tag{46}$$

This provides an alternative interpretation of the first term in Eq. 37 in terms of the velocity gradients at a stagnation point.

Combining the computations for the stretch factor of the two flowfields, we have the net result that the stretch factor for the present situation can be estimated as

$$K = \frac{3}{R} V_b + \frac{2}{R} V_r \tag{47}$$

where $V_b = U$ is the upward velocity and V_r is the effective radial velocity of the flame dR/dt. We estimate V_r by using Ross's experimental measurement of the horizontal flame motion and estimate the vertical rise velocity V_b by taking the difference between the vertical velocity determined in this experiment and Ross's value of V_r. Table 2 gives estimates of the stretch factor K for the 8%, 9%, and 10% flames. The values range from 28 s^{-1} to 40 s^{-1}, much smaller than the values of 500 to 1000 s^{-1} associated with extinction. Previous experiments on flame speed in lean hydrogen–air mixtures do not report the magnitude of the stretch factor. Our estimated values of the stretch factor are slightly smaller than the typical v alues of around 100 s^{-1} obtained by Egolfopoulus (1997) for lean methane–air flames. Of the total stretch factor, a maximum of 20 s^{-1} in the present experiments is due to buoyancy. This is a fairly modest amount of stretch and suggests that the difference between our results and Ronney's are primarily due to Ronney's use of the combustion inhibitor to visualize the flame. However, another difference is that in the prese nt experiments the flame accelerates nonuniformly and the baroclinic torque causes a non–uniform flow field within the flame. The effect of this nonuniform velocity field has not been quantified. More accurate data need to be obtained before any definitive statements can be made.

The estimated value of stretch is also much smaller than the amount of stretch required for extinction. Giovangigli and Smooke (1987) have computed the steady flame structure of lean hydrogen-air flames in a planar stagnation point flow. They found that for 9.3% H_2 that extinction occurred at a stretch of 1400 s^{-1}, and at 8.4 % H_2 that extinction occurred at a stretch of 500 s^{-1}.

An alternate measurement technique is diagrammed in Fig. 24; this is similar to the method used by Ross (1996). The horizontal growth of the flame front is tracked versus time and a linear fit produces a curve of the horizontal edge of the flame versus time. An alternative LDV measurement location would lie along this line. A two–component LDV measurement would allow one to test Ross's assumption of a stationary burned fluid and validate Ross's observation that the horizontal

% H_2	$r_{arrival}$	$t_{arrival}$	V_r	V_b	S_u	K
10	0.032 m	0.042 s	$\sim$ 0.45 m/s	0.12 m/s	0.12 m/s	40 s^{-1}
9	0.032 m	0.051 s	0.32 m/s	0.18 m/s	0.10 m/s	37 s^{-1}
8	0.035 m	0.07 s	0.18 m/s	0.21 m/s	0.08 m/s	28 s^{-1}

Table 2: Estimates of stretching factor in the present experiments.

growth of the flame kernel is unaffected by buoyancy. The implication of Ross's observation is that the vertical component of the velocity should be very small compared to the horizontal component. If this is what the LDV measurement implies, then there is a clear advantage to using this technique in that the strain would be due primarily to the radial expansion.

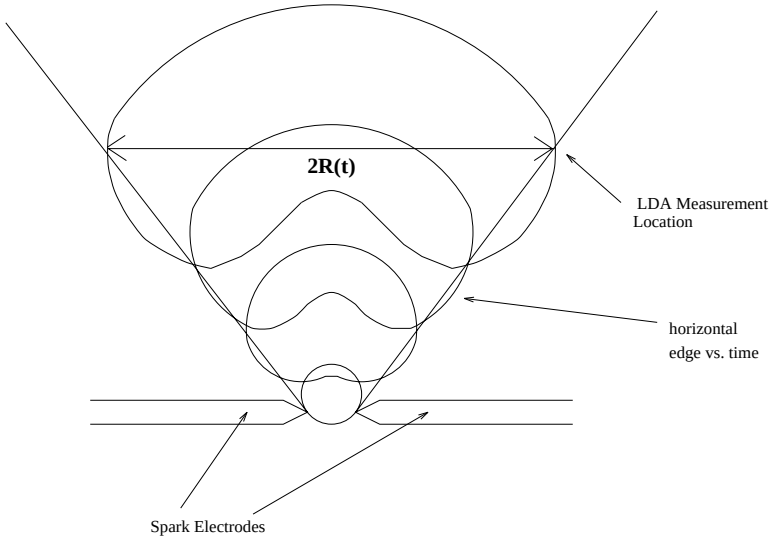

Figure 24: Suggested improved burning velocity measurement technique.

A large source of error in our lean measurements was the estimation of flame arrival time used to arrive at the results. One way to reduce this uncertainty is to redo the measurements at higher DAC gains with the goal of observing a velocity drop corresponding to the flame arrival. Another source of error was the independent experiments to determine V_f and u_u. Simultaneous measurement will allow self-consistent values for S_u. The four–beam photodiode system is more convenient to use with the LDV but it may be worthwhile to do a simultaneous LDV–schlieren measurement. Both methods suffer from the increased flame thickness at low burning velocities; however, consistently tracking either the outside or inside edge of the apparent flame front should give a reasonably accurate V_f if the reaction zone thickness does not change appreciably with time.

Flame thickness is an issue in any optical method used to measure V_f. For this reason, stationary flame methods, where $V_f \equiv 0$, may yield the most accurate results near the flammability limit. However, lean flames would be most sensitive to heat loss effects so burner methods may be unsuitable. If a stable flame can be maintained on a burner, then the stationary flame method is preferable to nonstationary methods. Near–limit hydrogen–air flames would be significantly more susceptible to heat loss effects than other flames because hydrogen burns at much leaner concentrations than other fuels due to its high diffusivity. For near–limit hydrogen–air flames, nonstationary methods may be the most appropriate.

For non-stationary flames, it has been suggested (Andrews and Bradley 1972) that the double–

kernel and measurement of the unburned fluid velocity are the two most promising techniques. For very lean flames, the double–kernel technique is poor although it works quite excellent near stoichiometric. The essence of the double–kernel technique is to measure V_f when $u_u = 0$ which happens when the two flame fronts coincide. However, if both flame fronts are poorly resolved due to a thick reaction zone, then one can imagine the difficulty in the technique.

Therefore, direct measurement of u_u and V_f appears to be the method of choice to measure S_u near the lean limit in a non–stationary flame (in normal gravity). The present experiment was one example of how this method can be implemented. From this experiment, it appears that the most promising method involves a simultaneous LDV-schlieren measurement where the horizontal growth of the flame front is tracked.

6 Summary and Suggestions for Future Work

The major results of this thesis are now summarized:

1. An LDV system was successfully assembled to measure fluid velocities in a combusting flow. When added to an existing schlieren system, it was now possible to measure the burning velocity. This type of approach appears to be method of choice for investigating the burning velocities of lean, non–stationary flames.

2. It was proposed that stationary methods, which are free from optical limitations encountered in nonstationary methods, are the most suitable methods for measuring the burning velocity of a general lean mixture. However, for near–limit hydrogen–air flames, nonstationary methods may be more suitable due to the difficulty in stabilizing a low temperature, slow burning, hydrogen–air flame on a burner.

3. Accurate measurements of the burning velocity were obtained for 9 and 10% H_2 mixtures. It was proposed that insufficient DAC gain was the problem in the leaner mixtures. Still, that an LDV signal was obtainable at the lean mixtures implies that this method may be able to generate useful data.

4. It was estimated that the strain for the experiments was modest and that the buoyancy contribution to S_u is relatively minor.

5. Several modifications of the experimental technique were suggested to improve the accuracy of the results.

6. It was experimentally observed that the transition to cellular instability for a H_2-air flame occurs between 9 and 10% H_2. It was also observed that the transition to downward propagation occurred between 8% and 9%.

Future work includes:

1. The measurements should be redone to see if insufficient DAC gain was the reason for the missing velocity drop at low H_2 concentrations.

2. LDV measurements will be made at different probe locations with a two–component system with frequency shift, the purpose being to investigate the flow field. A hypothesis is that a

vortex pair, caused by the gravitational field, causes the observed deformation of the flame surface (see figure 18).

7 Acknowledgments

This project began as a Caltech Summer Undergraduate Research Fellowhip (SURF) and the author was the recipient of the Lester Lees SURF fellowship in 1996. This work was also partially supported by Los Alamos National Laboratory under Contract 929Q0015-3A, DOE W-7405-ENG-36. The laser doppler velocimeter was generously donated by the late Prof. E. Zukoski. Dr. U. Pfahl and P. Svitek helped set up the combustion chamber and data acquisition system for these experiments. This study was carried out as a senior thesis under the supervision of Prof. J. E. Shepherd.

References

Andrews, G. E. and D. Bradley (1972). Determination of burning velocities: A critical review. *Combustion and Flame 18*, 133–153.

Barnard, J. A. and J. N. Bradley (1985). *Flame and Combustion* (2nd ed.). Chapman & Hall.

Coward, H. F. and G. W. Jones (1952). Limits of flammability of gases and vapors. Bulletin 503, Bureau of Mines.

Drain, L. E. (1980). *The Laser Doppler Technique*. John Wiley & Sons.

Durst, F., A. Melling, and J. H. Whitelaw (1976). *Principles and Practice of Laser–Doppler Anemometry*. Academic Press.

Egolfopoulos, F. N. (1997). Direct experimental determination of laminar burning velocity. In *Combustion Institute Western Sectional Meeting*.

Egolfopoulos, F. N. and C. K. Law (1990). An experimental and computational study of the burning rates of ultra-lean to moderately-rich $H_2/O_2/N_2$ laminar flames with pressure variations. In *Twenty-Third (International) Symposium on Combustion*. The Combustion Institute.

Gaydon, A. G. and H. G. Wolfhard (1960). *Flames – their stucture, radiation, and temperature* (2nd ed.). Chapman & Hall.

Giovangigli, V. and M. Smooke (1987). Extinction of strained premixed laminar flames with complex chemistry. *Combustion Science and Technology 53*, 23–49.

Hamamoto, Y., M. Izumi, E. Tomita, and O. Miyamoto (1991). Direct measurement of burning velocity of flame propagating in fuel-air homogeneous mixture in a closed vessel. *JSME International Journal 34*(2), 253–257.

Koroll, G. W., R. K. Kumar, and E. M. Bowles (1993). Burning velocities of hydrogen-air mixtures. *Combustion and Flame 94*, 330–340.

Law, C. K. (1988). Dynamics of stretched flames. In *Twenty-Second Symposium (International) on Combustion*, pp. 1381–1402.

Matalon, M. (1983). On flame stretch. *Combustion Science and Technology 31*, 169.

Pfahl, U. and J. E. Shepherd (1997). Flammability, ignition energy and flame speeds in NH_3–H_2–CH_4–N_2O–O_2–N_2 mixtures. Report FM97-4R1, Explosion Dynamics Laboratory, California Institute of Technology.

Reynolds, W. C. (1986). The element potential method for chemical equilibrium analysis: Implementation in the interactive program STANJAN. Technical report, Department of Mechanical Engineering.

Ronney, P. D. (1990). Near-limit flame structures at low Lewis number. *Combustion and Flame 82*, 1–14.

Ross, M. C. and J. E. Shepherd (1996). Lean combustion characteristics of hydrogen-nitrous oxide-ammonia mixtures in air. part I. Report FM96-4, Explosion Dynamics Laboratory, California Institute of Technology.

Turns, S. R. (1996). *An Introduction to Combustion*. McGraw–Hill.

van Wingerden, K. (1997). Review of data and models available at Christian Michelson Research for explosion hazard assessment. Report CMR-97-A40003, Christian Michelson Research AS.

VKI (1991). *Laser Velocimetry*. von Karman Institute for Fluid Dynamics 1991-05.

Westbrook, C. K. (1983). Numerical simulation of flame inhibition by CF_3Br. *Combustion Science and Technology 34*, 201–225.

Yariv, A. (1997). *Optical Electronics in Modern Communications* (5th ed.). Oxford University Press.

A Properties of Lean Hydrogen-Air Mixtures

Table 3 is a summary of STANJAN (Reynolds 1986) computations for lean hydrogen-air mixtures of concentrations ranging from 4% to 12% hydrogen molar concentration. Initial conditions were taken as 298 K and 1 atm. Some notes about table 3:

1. In all computations, the reactants were assumed to be H_2, O_2, and N_2 only. The allowed product species were taken as H, HO, H_2, H_2O, N, NO, NO_2, N_2, O, and O_2.
2. $\%H_2$ and $\%O_2$ are the percentage molar concentrations of hydrogen and oxygen respectively in the reactant mixture. $\%N_2$ can be determined by multiplying $\%O_2$ by 3.76.
3. ϕ is the equivalence ratio for the mixture (Turns 1996).
4. $(\frac{\rho_b}{\rho_u})_{adiab}$ is the density drop across the flame assuming an adiabatic (constant enthalpy), constant pressure combustion.
5. T_{adiab} is the adiabatic flame temperature.
6. P_{adiab} is the adiabatic explosion pressure computed assuming an adiabatic, constant volume combustion.
7. S_u is the burning velocity for the mixture. The values given are representative values measured in the present work.

$\%H_2$ (molar)	$\%O_2$ (molar)	ϕ	MW_u (kg/kmol)	ρ_u (kg/m^3)	MW_b (kg/kmol)	$(\frac{\rho_b}{\rho_u})_{adiab}$	T_{adiab} (K)	P_{adiab} (bar)	S_u (cm/s)
12	18.48	0.325	25.63	1.048	27.27	0.254	1254	4.00	
11	18.69	0.294	25.90	1.059	27.41	0.269	1173	3.77	
10	18.90	0.265	26.17	1.070	27.54	0.286	1097	3.54	12
9	19.11	0.235	26.43	1.081	27.68	0.306	1021	3.31	10
8	19.32	0.207	26.70	1.092	27.82	0.329	944	3.08	8
7	19.53	0.179	26.97	1.103	27.95	0.357	866	2.84	
6	19.74	0.152	27.24	1.114	28.08	0.390	787	2.60	5.5
5	19.95	0.125	27.51	1.125	28.21	0.432	708	2.35	4.5
4	20.16	0.099	27.78	1.136	28.34	0.485	627	2.09	

Table 3: Properties of lean hydrogen-air mixtures.

B Tables of Test Conditions and Experimental Settings

Tables 4 through 7 give the test conditions for each of the 104 experiments performed in this study. Runs 351–397 were diagnostic experiments to optimize the LDV system parameters and to establish an accurate method of filling. Runs 398–439 were LDV measurements from 4.2% to 10.1% H_2. Runs 440–454 were schlieren experiments in the same concentration range. Tables 8 and 9 gives the LDV and oscilloscope settings found optimal for this experiment. Notes about tables 4 through 7:

1. The "Run No" column refers to a specific run performed in either MCV or CONVOL since the two facilities were built.

2. The abbreviation "DR" in the "Comments" column stands for "data rate" and refers to the quality of the oscilloscope trace obtained from the DAC of the LDV Counter. The words "LDV trace" or "trace" are also used at times.

Run No	Date	Time	$\%H_2$ (molar)	P_{react} (kPa)	T_{react} (^{o}C)	Burn?	P_{prod} (kPa)	T_{prod} (^{o}C)	P_{max} (bar)	Comments
351	4/4/97	15:28	6.5	100.7	21.2	NO				dead volume
352	4/4/97	16:20	9.1	100.1	22.2	NO				dead volume
353	4/4/97	16:57	9.1	100.1	22.4	YES	88.0	22.5	3.20	
354	4/5/97	12:19	9.4	100.8	22.4	NO				dead volume?!
355	4/5/97	14:15	10.1	101.3	22.0	NO				dead volume?!
356	4/5/97	15:14	10.1	100.3	22.1	YES	88.0	24.0	3.78	
357	4/5/97	18:00	10.3	100.6	21.6	YES	88.3	22.6	3.64	
358	4/5/97	19:17	11.6	101.9	21.7	YES	85.0	22.3		nidaq failed
359	4/5/97	20:!2	12.0	102.5	21.9	YES	86.2	24.1	4.45	
360	4/5/97	21:23	11.1	101.3	21.9	NO				dead volume?!
361	4/6/97	13:17	10.1	100.1	21.7	YES	87.6	25.6	4.13	Tek failed
362	4/6/97	14:00	11.1	101.3	21.7	YES	86.5	25.0	4.36	
363	4/6/97	14:33	10.1	100.3	21.7	YES	87.6	23.4	4.04	
364	4/6/97	16:06	10.2	100.3	21.7	YES	87.4	22.9	4.19	
365	4/6/97	16:48	10.4	100.2	21.6	YES	87.0	22.2	4.21	good ldv trace
366	4/6/97	17:17	10.7	100.8	21.7	YES	86.8	22.7	4.36	good ldv trace
367	4/6/97	17:49	10.2	100.2	21.6	YES	87.0	21.7	4.06	decent ldv trace
368	4/6/97	18:20	10.4	100.5	22.2	YES	86.2	22.9	4.29	decent ldv trace
369	4/11/97	17:45	10.6	100.8	20.8	YES	86.9	20.7		trig too high
370	4/12/97	14:45	10.0	100.2	20.7	YES	87.3	21.3	4.14	trig too high
371	4/12/97	17:14	10.4	100.2	21.2	YES	80.8	21.7	5.10	too much fuel
372	4/12/97	17:48	10.1	100.2	21.6	YES	82.2	23.3	4.87	too much fuel
373	4/12/97	18:49	10.0	100.8	21.8	YES	87.9	23.5	4.16	trig too high
374	4/12/97	19:12	10.4	100.6	22.4	YES	86.9	23.2	4.19	Tek misfire
375	4/13/97	00:56	9.9	100.1	21.2	YES	87.9	23.5		Tek & nidaq failed
376	4/13/97	01:23	9.8	100.0	21.2	YES	86.8	21.6	3.99	DAC failed
377	4/13/97	03:13	10.1	100.2	21.3	YES	86.8	22.4	4.09	DAC failed
378	4/13/97	03:30	10.1	100.1	21.1	YES	87.0	22.6	4.07	worked!!
379	4/13/97	04:!2	10.1	100.1	21.4	YES	87.0	23.8	3.73	Tek failed
380	4/13/97	04:25	10.0	100.1	21.2	YES	86.5	22.5	4.08	poor DR

Table 4: Table of test conditions for MCV experiments 351–380

Run No	Date	Time	$\%H_2$ (molar)	P_{react} (kPa)	T_{react} (^oC)	Burn?	P_{prod} (kPa)	T_{prod} (^oC)	P_{max} (bar)	Comments
381	4/13/97	05:12	10.0	100.1	21.4	YES	86.9	23.2	4.06	decent ldv trace
382	4/13/97	05:44	10.0	100.0	21.6	YES	86.9	23.3	3.99	good ldv trace
383	4/13/97	06:11	9.8	100.1	21.5	YES	86.8	21.5	4.04	
384	4/13/97	06:39	9.8	100.1	21.6	YES	86.7	22.3	4.01	
385	4/13/97	06:55	8.9	100.2	21.6	YES	87.9	24.1	3.30	
386	4/13/97	07:19	9.0	100.1	21.6	YES	87.6	21.8	3.34	
387	4/13/97	07:45	9.0	100.0	21.7	YES	88.3	24.8	3.23	
388	4/13/97	08:00	9.0	100.2	21.9	YES	87.9	24.0	3.29	Tek misfire
389	4/13/97	08:16	9.3	100.4	22.0	YES	88.2	24.8	3.79	poor DR
390	4/13/97	09:00	8.9	100.1	21.7	YES	88.1	22.2	3.34	
391	4/13/97	09:44	9.0	100.1	21.6	YES	88.3	22.5	3.49	Tek misfire
392	4/13/97	10:01	9.1	100.1	21.6	YES	87.5	21.7		poor DR
393	4/13/97	10:35	9.1	100.1	21.1	YES	88.2	22.5	3.58	Tek failed
394	4/13/97	10:49	9.0	100.2	21.1	YES	88.4	22.3	3.50	Tek failed
395	4/13/97	11:08	9.2	100.4	21.2	YES	87.3	21.2	3.51	excellent ldv trace
396	4/13/97	20:10	10.1	100.2	21.3	YES	86.8	26.7	4.13	good ldv trace
397	4/13/97	20:39	9.9	100.0	21.6	YES	86.7	23.6	4.13	longer record
398	4/13/97	20:43	9.8	100.0	22.2	YES	87.3		4.08	magnificent trace!!
399	4/13/97	21:41	10.1	100.1	22.2	YES	86.7	29.3	4.16	excellent trace
400	4/13/97	22:16	9.9	100.0	22.4	YES	86.9	34.7	4.09	excellent trace
401	4/13/97	22:35	9.1	100.1	22.4	YES	88.5	25.1	3.43	excellent trace
402	4/13/97	22:49	9.1	100.2	22.3	YES	88.1	28.3	3.48	good trace
403	4/14/97	23:16	9.0	100.1	22.9	YES	88.1	31.7	3.39	excellent trace
404	4/14/97	03:24	9.2	100.2	21.6	YES	88.5	49.3	3.55	
405	4/14/97	03:48	7.9	100.1	22.1	YES	95.0	36.7	1.83	
406	4/14/97	04:03	7.8	100.0	22.1	YES	96.4	31.9	1.67	
407	4/14/97	04:15	8.2	100.3	21.8	YES	94.6	39.2	1.82	
408	4/14/97	04:29	8.0	100.1	22.7	YES	95.4	37.8	1.79	
409	4/14/97	04:42	7.0	100.1	22.4	YES	97.7	25.3	1.48	
410	4/14/97	04:55	6.9	100.2	22.1	YES	97.9	22.1	1.47	

Table 5: Table of test conditions for MCV experiments 381–410

Run No	Date	Time	%H_2 (molar)	P_{react} (kPa)	T_{react} (^oC)	Burn?	P_{prod} (kPa)	T_{prod} (^oC)	P_{max} (bar)	Comments
411	4/14/97	05:08	6.8	100.0	22.1	YES	97.9	23.9	1.39	Tek error
412	4/14/97	05:23	7.2	100.2	22.5	YES	97.5	26.2	1.60	
413	4/14/97	05:40	7.0	100.2	22.7	YES	97.8	24.4	1.44	
414	4/14/97	05:49	7.0	100.2	22.6	YES	97.7	27.4	1.50	
415	4/14/97	06:07	6.0	100.0	22.7	YES	99.0	22.3	1.27	poor DR
416	4/14/97	06:14	6.0	100.3	22.4	YES	99.2	22.7	1.21	better DR
417	4/14/97	06:25	6.1	100.3		YES	99.1	22.2	1.27	
418	4/14/97	06:41	6.1	100.1	22.4	YES	99.0	22.5	1.31	
419	4/14/97	06:59	5.1	100.3	22.4	YES	99.7	22.3	1.18	
420	4/14/97	07:09	5.2	100.2	22.4	YES	99.4	22.2	1.28	
421	4/14/97	07:25	4.9	100.1	22.3	YES	99.7	22.3	1.28	
422	4/14/97	07:42	5.1	100.2	22.3	YES	99.7	22.3	1.26	good DR
423	4/14/97	08:03	4.1	100.3	22.3	NO				too lean
424	4/15/97	01:01	4.8	100.3	20.6	YES	99.4	20.6	1.31	poor DR
425	4/15/97	01:13	4.8	107.1	20.6	YES	107.0	20.6	1.39	poor DR
426	4/15/97	01:52	4.7	100.2	20.6	YES	99.9	20.8	1.20	great DR
427	4/15/97	02:10	4.7	100.3	20.8	YES	99.9	20.8	1.26	great DR
428	4/15/97	02:35	4.5	100.1	20.8	YES	99.9	20.8	1.26	
429	4/15/97	02:57	4.8	100.3	21.0	YES	99.9	21.0	1.34	
430	4/15/97	03:20	4.5	100.1	21.1	YES	99.8	21.0	1.30	great DR
431	4/15/97	03:37	4.2	100.2	21.1	YES	100.1	21.1	1.23	good DR
432	4/15/97	03:50	4.6	100.6	21.1	YES	100.4	21.1	1.20	
433	4/15/97	04:04	4.7	100.6	20.9	YES	100.3	20.9	1.22	Tek error
434	4/15/97	04:25	4.4	100.3	21.0	YES	100.1	21.2	1.28	nidaq missing!?
435	4/15/97	04:50	4.6	100.7	20.8	YES	100.7	20.8	1.29	
436	4/15/97	05:07	4.4	100.2	20.9	YES	99.9	20.9	1.37	
437	4/15/97	05:20	4.1	100.1	21.0	YES	100.0	20.9	1.20	very poor DR
438	4/15/97	05:32	4.5	100.5	20.9	YES	100.1	20.9	1.16	
439	4/15/97	05:56	4.2	100.0	20.9	YES	99.8	20.9	1.14	
440	4/23/97	05:08	10.1	100.1	22.4	YES	87.5	23.8	3.78	1st schlieren

Table 6: Table of test conditions for MCV experiments 411–440

Run No	Date	Time	%H_2 (molar)	P_{react} (kPa)	T_{react} (^{o}C)	Burn?	P_{prod} (kPa)	T_{prod} (^{o}C)	P_{max} (bar)	Comments
441	4/23/97	05:35	9.1	100.1	23.0	YES	88.3	24.2	3.29	nidaq missing!?
442	4/24/97	01:40	10.0	100.0	22.8	YES	86.9	22.6	3.91	cellular instability
443	4/24/97	04:05	9.0	100.0	23.5	YES	88.1	22.9	3.19	
444	4/24/97	04:22	8.0	100.0	23.0	YES	94.2	23.5	1.76	upward flame
445	4/24/97	04:41	7.1	100.2	22.9	YES	96.9	22.9	1.57	
446	4/24/97	05:18	6.1	100.1	23.1	YES	98.9	23.5	1.24	
447	4/24/97	05:33	5.0	100.0	23.7	YES	99.3	23.5	1.16	
448	4/24/97	05:49	4.6	100.1	23.8	YES	99.7	23.3	1.12	
449	4/24/97	06:00	4.3	100.1	23.1	YES	99.8	23.2	1.09	
450	4/24/97	06:28	4.7	100.0	23.6	YES	99.6	23.4	1.11	
451	4/24/97	06:50	8.7	100.2	23.8	YES	88.3	23.6	3.06	two–legged wake
452	4/24/97	07:03	8.4	100.2	23.8	YES	89.0	23.5	2.6	two–legged wake
453	4/24/97	07:21	8.2	100.0	23.6	YES	91.8	23.9	1.9	small two–legged wake
454	4/24/97	07:33	8.1	100.0	23.8	YES	91.9	24.4	1.9	one–legged wake

Table 7: Table of test conditions for MCV experiments 440–454

Table 8: DANTEC 55L90a Counter Processor settings

Amplifier Gain	−7 dB
Comparator Accuracy	12%
DAC Gain	10
Mode	Fixed N_f
Pass Band	4–256 kHz
PM Type	57x08 with built–in preamp
PM Gain	1.7 kV
Preamp Gain	0 dB
Threshold Level	31 dB

Table 9: Tektronix TDS 460A Oscilloscope settings

Pretrigger	0%
Record Length	30000 points
Sampling Rate	100 kS/s
Trigger Level	1.8 V
Trigger Source	Filtered PM signal, “Monitor Out”